Materials Advances

ROYAL SOCIETY OF CHEMISTRY

PAPER

View Article Online
View Journal | View Issue

Cite this: *Mater. Adv.*, 2025, 6, 6803

Annealing $BaAl_2O_4:Tb^{3+}/Tb^{4+}$ in air and a reducing atmosphere: a strategy to enhance luminescence by eliminating Tb^{4+}

Divya Janardhana, Shivaramu Nagarasanakote Jayaramu,* Elizabeth Coetsee, David E. Motaung and Hendrik C. Swart*

The enhancement of green luminescence in terbium (Tb)-doped $BaAl_2O_4$ phosphors was significantly influenced by the annealing environment, primarily due to the reduction of Tb^{4+} to Tb^{3+} – a key factor for solid-state lighting applications. In this research, $BaAl_2O_4:Tb^{3+}/Tb^{4+}$ luminescent materials were synthesized through a coprecipitation method. The sample underwent annealing at 1200 °C for 2 h in an alumina crucible in air and under varying pressures of a H_2 (5%)/Ar atmosphere to investigate the influence of annealing at different atmospheres on the luminescent characteristics of $BaAl_2O_4:Tb^{3+}$. X-ray powder diffraction analysis of Tb^{3+}-doped $BaAl_2O_4$ revealed a hexagonal crystal structure, corresponding to the space group $P6_3$. X-ray photoelectron spectroscopy (XPS) showed that Ba atoms occupied two distinct sites in $BaAl_2O_4$. Additionally, the XPS analysis confirmed the presence of both Tb^{3+} and Tb^{4+} oxidation states in the $BaAl_2O_4$:Tb sample annealed in air, which is further supported by electron paramagnetic resonance analysis, substantiating the presence of Tb^{4+}. The samples annealed in a H_2 (5%)/Ar atmosphere demonstrated superior photoluminescence (PL) relative to those annealed in air, attributable to the absence of Tb^{4+} in the samples. PL emission in blue, green, and red was observed under excitation from the interconfigurational $4f^8 \rightarrow 4f^7\,5d^1$ transitions of Tb^{3+} (228 nm). UV-Vis diffuse reflectance studies indicated the nonexistence of Tb^{4+} in samples annealed in a H_2 (5%)/Ar environment at varying pressures. These investigations suggest that the presence of Tb^{4+} in $BaAl_2O_4$ functions as a luminescence quencher for Tb^{3+}, presumably due to charge compensation and electron acceptor defects that inhibit the luminescence of Tb^{3+}.

Received 14th July 2025,
Accepted 12th August 2025

DOI: 10.1039/d5ma00747j

rsc.li/materials-advances

1. Introduction

Alkaline earth aluminates are adaptable luminous materials with significant potential for various applications. They can be synthesized using many processes, each providing distinct advantages for temperature regulation and material properties. These compounds are exceptionally well known for their excellent luminescent properties, as well as their thermal and chemical stability,[1] and thus these compounds can be termed as promising candidates for the use in solid-state lighting,[2,3] radiation dosimetry and smart materials.[4,5] This family is characterized by metal oxides with the general formula of AB_2O_4, where A and B denote divalent and trivalent cations, respectively. This crystal structure enables both divalent and trivalent activators to be integrated without significantly disturbing the oxidation states of the host matrix. However, charge compensation is required when a trivalent ion is incorporated at the A-site. This often leads to the formation of oxygen interstitials that can act as a trapping center within the band-gap of the host. Co-doping with both types of ions (divalent and trivalent ions) offers a practical approach to enhance the emission behaviour, enabling color modulation or white-light emission, making these materials suitable for white-light LEDs and other optoelectronic devices.[6] These compounds are usually represented by the formula MAl_2O_4 (M = Mg, Ba, Ca, Sr, or Be), and these compounds exhibit typical luminescence behavior that is highly dependent on both dopant selection and the synthesis method employed.[7]

$BaAl_2O_4$ has been studied as a favorable host material for rare-earth (RE) doping due to its wide band gap, and high refractive index. The incorporation of rare earth (Eu^{3+}, Eu^{2+}, Pr^{3+}, Sm^{3+}, Dy^{3+}, Tb^{3+}) elements[8] or transition (Cr^{3+}) metal[9] plays a crucial role in determining the emission behavior of these hosts. These activators introduce localized electronic states within the band gap of the host material, enabling a wide range of emissions depending on their oxidation state, site symmetry, interaction with the crystal field and an efficient

Department of Physics, University of the Free State, Bloemfontein ZA-9300, South Africa. E-mail: swarthc@ufs.ac.za, nj.shivaram@gmail.com

energy transfer between the host and activators.[10] This enhances their luminous characteristics, rendering them ideal for sophisticated lighting, display technologies, and various optoelectronic devices.[3,11–13]

RE elements are widely used for visible light emission in solid-state lighting, display, and emergency signage. In contrast, Bi^{3+} exhibits significant emission in the UV region, with applications in sterilization and photocatalysis. Cr^{3+} typically shows narrow emission around 701 nm but also emits broadband emission in the near-infrared (NIR) region with weak crystal field hosts for bio-imaging and optical communications.[9,14] Thus, control of the emission properties of $BaAl_2O_4$ phosphors *via* strategic doping is imperative in creating multifunctional luminescent materials. X. Yin *et al.*[3] reported on cyan phosphor ceramics $Ba_{1-x}Al_2O_4$:xEu^{2+} (x = 0.005–0.1), which were synthesized using high-temperature vacuum sintering. The $BaAl_2O_4$:Eu^{2+} phosphor ceramics demonstrated a broad emission band with a peak at 497 nm upon excitation with 365 nm near-ultraviolet light. White LEDs constructed with these phosphor ceramics emitted white light with a correlated color temperature (CCT) of 5050 K and a color rendering index (CRI) of 75, indicating their suitability for full-spectrum lighting applications.[3] $BaAl_2O_4$:Eu phosphors exhibit two luminescence centers from different Ba sites. The primary emission at 611 nm is due to the Eu^{3+} electric dipole transition ($^5D_0 \rightarrow {}^7F_2$). Broad emission at 500 nm arises from the Eu^{2+} ($4f^6\ 5d^1 \rightarrow 4f^7$) transition, while peaks at 576, 596, 654, and 702 nm correspond to Eu^{3+} 4f–4f transitions.[15]

Tb^{3+} is a well-known activator for green-emitting phosphors and has been widely used in tricolor white light-emitting diodes.[16] Tb^{3+}-doped barium aluminates and related compounds demonstrate exceptional luminous characteristics, making them potential candidates for phosphor applications. These materials exhibit intense green emission upon UV excitation, principally attributed to the $^5D_4 \rightarrow {}^7F_j$ (j = 0–6) transitions of Tb^{3+} ions.[17,18] The photoluminescence spectra generally exhibit significant peaks at approximately 484, 540, 589, and 612 nm, with the 540 nm emission being the most prominent.[17,19] Luminescence quenching in Tb^{3+}-doped materials may arise *via* several causes, including the oxidation of Tb^{3+} to the non-luminescent Tb^{4+} state.[18,20] Annealing in a reducing environment has been shown to enhance Tb^{3+} ion luminescence and prevent Tb^{4+} ion generation in several materials. Zhang *et al.*[21] developed a dual-annealing post-treatment approach for Tb:Y_2O_3 transparent ceramics, eliminating Tb^{4+} ion-related coloration. This technique significantly increased photoluminescence and radioluminescence production by inhibiting the production of non-luminescent Tb^{4+} species. The dual-annealing process involved converting Tb element from Tb^{4+} to Tb^{3+} in a reducing atmosphere, followed by a subsequent annealing treatment to improve the ceramic structure and ion luminous efficiency.[21] A. V. Myshkina *et al.*[22] propose that the reduction of Ce^{4+} to Ce^{3+} during annealing in a reducing environment enhances the material's luminescent properties.[22]

The low-temperature thermoluminescence (TL) glow peaks (typically below 150 °C) correspond to shallow traps, which are considered less stable, fade rapidly, and contribute to persistent luminescence.[23,24] In contrast, the high-temperature TL glow peaks (usually above 150 °C) correspond to deeper traps, which are more stable, fade more slowly, and are better suited as storage energy for dosimetry applications. L. C. V. Rodrigues *et al.*[25] reported the TL glow curves of $BaAl_2O_4$:Eu^{2+},Dy^{3+} materials synthesized by the solid-state method exhibit a strong band around 70 °C, along with weaker bands at 120 °C and 200 °C, attributed to electron and/or hole traps within the host's energy gap. Manaka *et al.*[26] observed a TL glow curve with a prominent peak around 114 °C, and two weaker peaks at 186 °C and 292 °C for Mn-doped $BaAl_2O_4$ phosphors. J. Du and D. Poelman[27] reported that Cr^{3+}-doped $Mg_{1+x}Ga_{2-2x}Ge_xO_4$ phosphors exhibit strong NIR afterglow at extremely low temperatures (−80 °C) rather than at room temperature, due to their ability to stabilize a large number of shallow traps at −80 °C, as confirmed by TL analysis. Thermoluminescence is an extremely sensitive technique to determine the character of traps. Trap parameters and kinetic values depend on various parameters such as type and concentration of dopants, synthesis processes, annealing processes, and so on.[28,29]

Various methods have been employed for the synthesis of rare-earth-doped $BaAl_2O_4$, including sol–gel,[17] solution combustion synthesis,[15] high-temperature vacuum sintering,[3] solid-state reaction,[8] co-precipitation,[30] and facile solvothermal methods.[31] Among these, the co-precipitation method is a simple and most commonly used method for producing many materials such as phosphors, nanoparticles, and semiconductors.[32] It possesses homogeneous control over the particle size, high thermal stability, composition, and purity control parameters, and can be used both for small-scale laboratory synthesis and industrial-scale synthesis.[33,34] The process is simple and can be tailored by variable temperature, pH, and precursor concentration control. It is environmentally friendly, particularly as it requires little energy and uses aqueous solutions instead of organic solvents.[34,35] Research has shown that the coprecipitation process can be scaled up from a small quantity of 176 mL to larger amounts of around 100 L total volume.[32,33] One of the advantages of co-precipitation is that it may be performed at relatively low processing temperatures and has a short processing time. Consequently, production is less expensive, and it is possible to produce high-purity materials and tunable morphologies.[36] This method allows for the use of non-toxic materials, produces minimal hazardous waste, and enables lower sintering temperatures, reducing energy consumption and overall cost.[37] However, the present study looked at how the annealing atmosphere changes the optical properties of $BaAl_2O_4$:Tb^{3+}/Tb^{4+}, which was made using the coprecipitation method. This work mainly focused on the enhancement of green luminescence in Tb-doped $BaAl_2O_4$ phosphors, which is significantly influenced by the annealing environment, primarily due to the reduction of Tb^{4+} to Tb^{3+} under reducing (5% H_2/Ar) conditions, a key factor for solid-state lighting applications. The effects of this modification were systematically investigated and correlated with the material's structural, morphological, optical, photoluminescence, and thermoluminescence characteristics.

2. Experimental section

2.1. Materials and preparation

The coprecipitation method was used to successfully synthesize $BaAl_2O_4$:Tb (1 mol%). Ba $(NO_3)_2$ (2.5 g) and 50 ml of water were added, and the temperature was maintained at 75 °C. Then $Al(NO_3)_3$ (7.50 g) was added after complete dissolution, and then $Tb(NO_3)_2$ (0.043 g) was added. After that, the temperature was reduced to 50 °C. After that, ammonium bicarbonate was used to adjust the pH to 11 until the white precipitate forms, and then the obtained precipitate is centrifuged and dried at 110 °C overnight. Then annealed at different pressures in a 5% H_2/Ar atmosphere and in air at 1200 °C. A detailed schematic representation of the synthesis process of Tb-doped $BaAl_2O_4$ phosphor is shown in Fig. 1.

2.2. Characterizations

The crystal structure of the prepared materials was analyzed using XRPD patterns. The XRPD data were recorded at room temperature (RT) using a Bruker D-8 Advance (Germany) powder X-ray diffractometer, equipped with Cu Kα_1 radiation (λ = 1.5406 Å) operated at 40 kV and 40 mA, over a 2θ range of 15° to 80°. The surface morphology and microstructure of the $BaAl_2O_4$:Tb samples were characterized using a field-emission scanning electron microscope (FE-SEM, JEOL JSM-7800F, Japan). Elemental materials were analyzed using an energy-dispersive X-ray spectroscopy (EDS) system attached to the FE-SEM. The surface chemical composition was analyzed by XPS using a PHI 5000 Scanning ESCA Microprobe, equipped with a monochromatic Al K_α X-ray source (1486.6 eV), at RT. The high-resolution XPS spectra were fitted using the XPS peak fit 41, employing Gaussian–Lorentzian line shapes and iterated-Shirley background subtraction. The diffuse reflectance infrared Fourier transform (DRIFT) spectra of $BaAl_2O_4$:Tb^{3+} were recorded using a Nicolet 6700 spectrometer (Thermo Scientific) equipped with a smart diffuse reflectance accessory. The diffuse reflectance (DR) spectra were recorded using a UV-vis-NIR spectrometer (PerkinElmer Lambda 950, USA) over the wavelength range of 200–800 nm, employing a 150 mm diameter integrating sphere and $BaSO_4$ powder as the standard reference.

Photoluminescence excitation (PLE) and emission (PL) spectra were obtained at room temperature using a Varian Cary Eclipse fluorescence spectrophotometer (Agilent Technologies, USA), which utilizes a 150 W xenon (Xe) lamp as the excitation source. The colour chromaticity coordinates of the $BaAl_2O_4$:1 mol% Tb^{3+} phosphors were performed using an Osram-Sylvania colour calculator (GOCIE-V2, CIE-1931) programme. The PL lifetime of the $^5D_4$ level of Tb^{3+} emission in $BaAl_2O_4$:1 mol% Tb^{3+} phosphors was analysed using a FS5 Spectrofluorometer (Edinburgh, UK) at RT. The phosphors' PL quantum yield (PLQY) was measured using an Edinburgh FLS980 spectrometer, equipped with an integrating sphere, employing the direct excitation method.

X-band EPR measurements were performed in a JEOL, JES FA-200 spectrometer equipped with an Oxford ESR900 gas-flow cryostat and a Scientific Instruments 9700 temperature controller. The microwave power remained constant at 30 mW, and the frequency remained steady at 9.4 GHz. The TL measurements were recorded over the 30–460 °C temperature range at a constant heating rate of 5 °C s^{-1} using a TL reader (model: TL/OSL 1008; Nucleonix Systems, India). Before the measurements, the specimens were irradiated using an 8 W UV lamp emitting at 254 nm. The unresolved glow curves were deconvoluted using glow curve deconvolution (GCD) analysis, employing a general-order kinetic function.

3. Results and discussion

3.1. Structural interpretation of Tb doped $BaAl_2O_4$

The XRPD patterns of the 1 mol% Tb^{3+}-doped $BaAl_2O_4$ (Fig. 2(a)) demonstrated that the materials exhibit a hexagonal

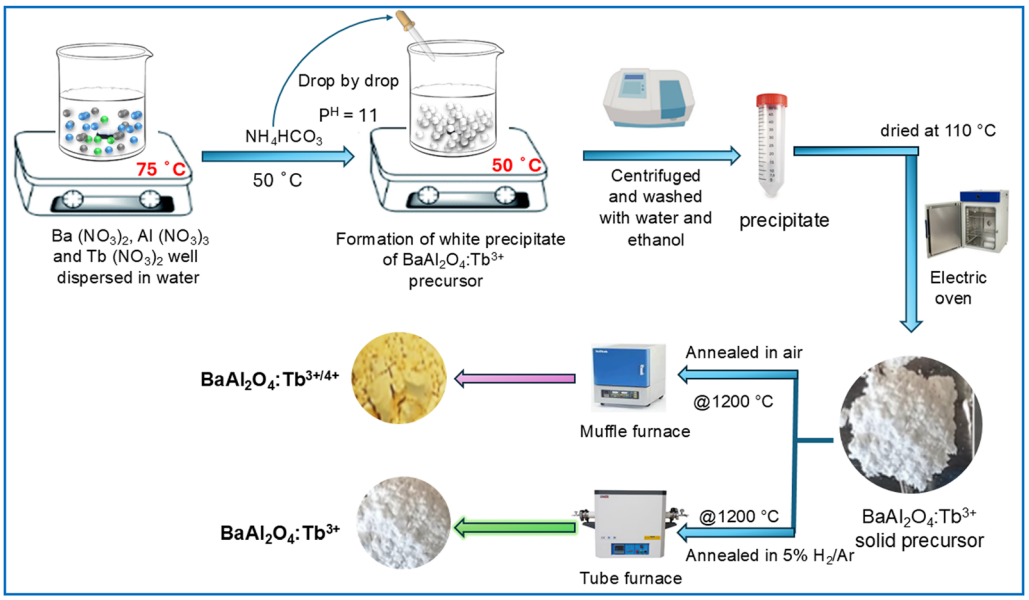

Fig. 1 Schematic representation of the synthesis of Tb-doped $BaAl_2O_4$ phosphor.

crystal structure with the space group $P6_3$ (COD #2002225)[38] for samples annealed in air and an H_2 (5%)/Ar environment, with pressure ranging from 60 to 200 kPa. The XRPD patterns for the 1 mol% Tb^{3+}-doped $BaAl_2O_4$ samples exhibited no contaminants or residual materials in any of the samples. The XRPD pattern of Tb-doped $BaAl_2O_4$ annealed at 1200 °C for 2 h in air shows a shift of the main diffraction (102) plane at 28.2° toward higher 2θ angles compared to the calculated (standard) pattern of undoped $BaAl_2O_4$. This shift is attributed to substituting two Tb^{3+} ions (1.10 Å in nine-fold coordination) for two Ba^{2+} ions (1.47 Å), leading to lattice contraction. Although charge imbalance resulting from substituting Tb^{3+} for Ba^{2+} would typically be compensated by forming oxide interstitials—potentially leading to expansion of the unit cell volume[18]—such expansion was not observed in this study. Instead, a contraction of the unit cell volume was detected, suggesting the coexistence of Tb^{3+} and Tb^{4+} ions within the lattice. This may cause inhomogeneous redistribution of Tb ions across the two crystallographic Ba sites.[39] The presence of Tb^{3+} and Tb^{4+} ions at Ba^{2+} sites was further confirmed by X-ray photoelectron spectroscopy (XPS). In addition, UV-visible diffuse reflectance spectroscopy supported the mixed-valence nature of Tb ions. The XRPD diffraction peaks for the material annealed in a reducing environment shifted to lower 2θ angles than those annealed in air (Fig. 2(b)). The shift to lower 2θ angles continued up to 200 kPa, reducing pressure. This shift is due to the reduction of Tb^{4+} to Tb^{3+} ions, and the ionic radii of Tb^{3+} (1.10 Å with a coordination number of 9) are relatively high compared to that of Tb^{4+} (0.8–0.9 Å).[40] Hence, the lattice parameters of $BaAl_2O_4$ underwent expansion, see Table 1. Bragg's law posits that an increase in ionic radii results in a rise in interplanar distance d, thereby causing a shift of the diffraction peaks to a lower 2θ angle. This indicates the enlargement of the lattice parameters resulting from the increased content of Tb^{3+} ions.

Fig. 2(c) illustrates the Rietveld refinement of the XRPD patterns at ambient temperature for Tb^{3+} (1 mol%) doped $BaAl_2O_4$ powder. Rietveld refinement investigations[19] indicate that incorporating Tb^{3+} ions (1 mol%) into the crystal structure of $BaAl_2O_4$ likely results in substituting Ba^{2+} cation sites. The Rietveld refinements were performed on the XRPD data for the aluminates utilizing a hexagonal system with space group $P6_3$ (COD #2002225).[38] The fitting value, R_{wp}, is 9.9% for the Tb^{3+}-doped $BaAl_2O_4$, signifying a strong concordance between the experimental and computed data.

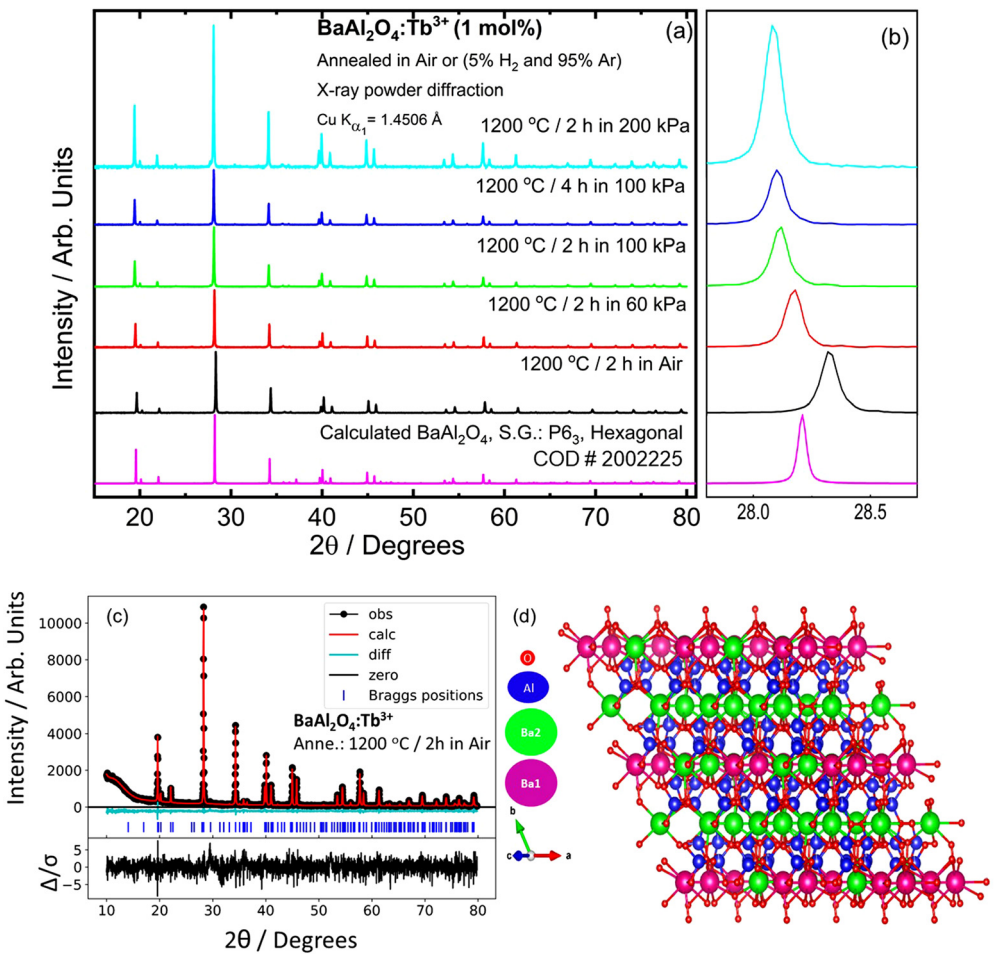

Fig. 2 (a) PXRD profiles and (b) (201) reflection of $BaAl_2O_4$:Tb (1 mol%) phosphors annealed in air and selected pressures of H_2 (5%)/Ar reduced atmosphere. Rietveld PXRD profiles of $BaAl_2O_4$:Tb (1 mol%) phosphors annealed in air (c) and (d) spatial structure of the $BaAl_2O_4$ unit cell.

Table 1 Crystal lattice parameters of $BaAl_2O_4$:Tb (1 mol%) phosphors annealed in air and under a reducing atmosphere

Sample	Lattice parameters		
	a/Å	c/Å	Volume (V) in Å^3
Air	10.4415 ± 0.0003	8.7865 ± 0.0005	829.6054 ± 0.0526
60 kPa	10.4599 ± 0.0002	8.8113 ± 0.0004	834.8854 ± 0.0448
100 kPa 2 h	10.4692 ± 0.0002	8.8221 ± 0.0004	837.3862 ± 0.0450
100 kPa 4 h	10.4712 ± 0.0002	8.8245 ± 0.0004	837.9516 ± 0.0450
200 kPa 2 h	10.4731 ± 0.0002	8.8255 ± 0.0004	838.3431 ± 0.0451
Standard ($P6_3$)[38]	10.47000	8.81900	837.2273

The detailed unit cell characteristics for Tb^{3+}-doped $BaAl_2O_4$ are as follows: $a = b = 10.4717$ Å, $c = 8.8133$ Å, unit cell volume (V) = 836.953 Å^3, and the density is 4.120 g cm^{-3}. The crystallographic structure of the $BaAl_2O_4$ unit cell was depicted utilizing the visualization for electronic and structural analysis (VESTA) software, version 3 (Copyright (C) 2006–2021, Koichi Momma and Fujio Izumi), as illustrated in Fig. 2(d).

3.2. Microstructure and elemental analysis

The morphologies of Tb^{3+}-doped $BaAl_2O_4$ powders, annealed in air and at 100 kPa pressure in a H_2 (5%)/Ar gas mixtures environment, obtained *via* the coprecipitation process, are illustrated in Fig. 3(a) and (d), respectively. The Tb^{3+}-doped $BaAl_2O_4$ nanoparticles produced during coprecipitation have a nearly hexagonal morphology, are tightly aggregated, and are irregularly distributed on the surface. However, the boundaries of individual particles are distinctly identifiable. Moreover, tiny nanocrystals are uniformly dispersed across the whole surface of the particles in both samples, annealed in air and a H2 (5%)/Ar gas mixture environment. The hexagonal structures are ascribed to the $BaAl_2O_4$ phase, as confirmed by the XRPD data shown in Fig. 2(a). The emergence of white particles on bigger particles, as shown in the FESEM images, might be ascribed to a precipitation or crystallization process occurring during sample preparation at high annealing temperature.[15] The bright white particles observed during FESEM imaging indicate surface charging caused by the interaction of the electron beam with the material surface. This fact implies that the white particles are charged.[41]

The mean particle sizes of the samples annealed in air and the H_2 (5%)/Ar gas mixtures environment (100 kPa) are 225 nm and 297 nm, respectively, Fig. 3(b) and (e). The increased particle size in the sample annealed in a H_2 (5%)/Ar gas mixture, compared to that annealed in air, is due to the expansion of the Tb^{3+}-doped $BaAl_2O_4$ lattice during the annealing process in the H_2 (5%)/Ar gas mixture, as supported by the XRPD results. Fig. 3(c) and (f) present the EDS data for the Tb^{3+}-doped $BaAl_2O_4$ samples annealed in air and an Ar environment, respectively. The elements barium (Ba), oxygen (O), aluminum (Al), and terbium (Tb) were identified in the EDS spectra. The existence of Tb confirmed the successful incorporation of Tb^{3+} into the $BaAl_2O_4$ lattice.

3.3. UV-visible diffuse reflectance spectroscopy (UV-DRS)

Fig. 4(a) displays the UV-vis diffuse reflectance spectra of Tb^{3+}-doped $BaAl_2O_4$ powder samples annealed in air and H_2 (5%)/Ar

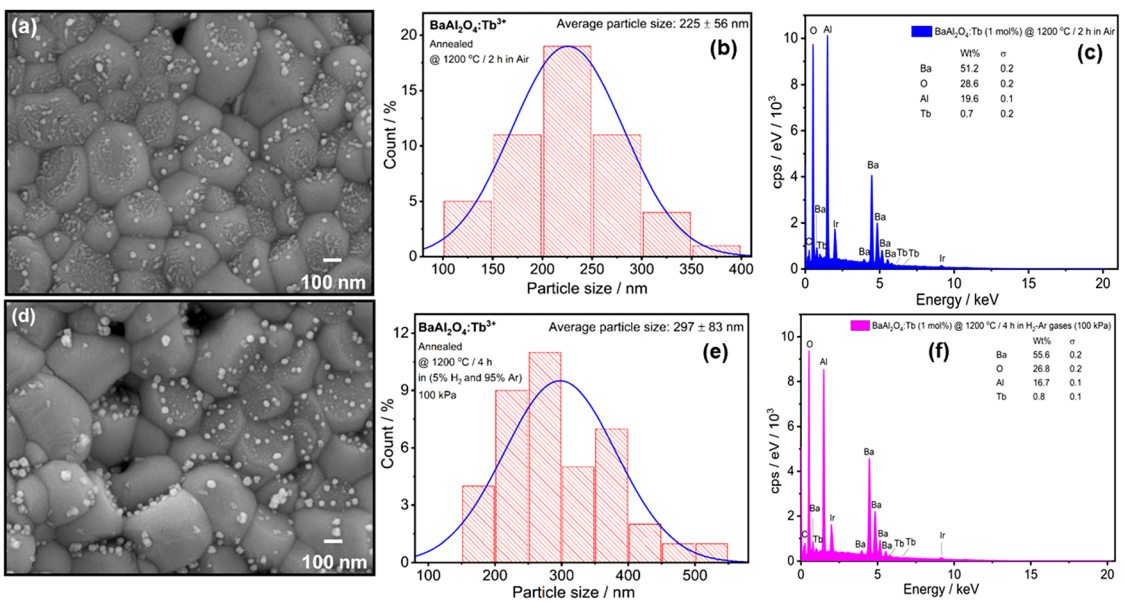

Fig. 3 SEM micrographs (a) and (d), particle size distribution (b) and (e), and EDS (c) and (f) of $BaAl_2O_4$:Tb (1 mol%) phosphors annealed in air and 100 kPa pressure of H_2 (5%)/Ar reduced atmosphere.

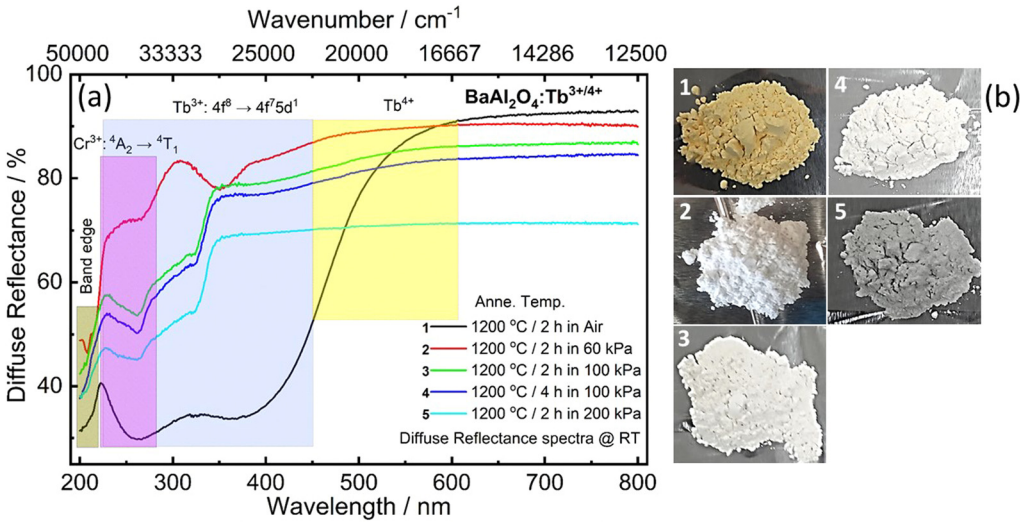

Fig. 4 (a) Room temperature diffuse reflectance spectra and (b) visible powder color under the fluorescent lamp of $BaAl_2O_4$:Tb^{3+} (1 mol%) phosphors annealed in air and selected pressures of a H_2 (5%)/Ar reduced atmosphere.

atmospheres. The spectra of the Tb^{3+}-doped $BaAl_2O_4$ sample display a significant reflection band at 210 nm, attributed to the bandgap of the Tb^{3+}-doped material. A diminished reflectance band detected at 267 nm corresponds to Cr^{3+} contaminants within the aluminum component of the sample.[18] The Cr ion impurity generally originates from the aluminum source, as trace amounts of Cr are commonly found in aluminum compounds. Therefore, the Cr^{3+} may have been unintentionally incorporated into the $BaAl_2O_4$ lattice from the $Al(NO_3)_3{\cdot}9H_2O$ raw material used during material preparation.[42] However, Cr was not intentionally added, and its concentration is negligible relative to the primary dopants discussed in this study. The presence of Cr^{3+} impurities was also reported in undoped $SrAl_2O_4$ by Vitola *et al.*,[42] where the impurity was attributed to the Al_2O_3 source used during synthesis. Furthermore, absorption bands within the 330–385 nm range are associated with the $4f^8 \rightarrow 4f^75d^1$ electronic transition of Tb^{3+} ions.[43] A supplementary absorption band between 450 and 600 nm is detected in the sample annealed in air (oxidizing environment). This band results from the presence of Tb^{4+} ions.[18,44] A characteristic peak of this absorption band is observed during annealing in air, which is attributed to the oxidation of certain Tb^{3+} ions to Tb^{4+} ions. This indicates that the host crystal possesses a minor quantity of Tb^{4+} ions. In contrast, the sample annealed in an argon atmosphere exhibits no absorption bands in this region, so confirming the elimination of Tb^{4+} in the H_2 (5%)/Ar-annealed samples, as Tb^{4+} ions were reduced to Tb^{3+} ions during annealing in the H_2 (5%)/Ar mixture atmosphere.[45] The presence of Tb^{4+} ions in the material annealed in air is evidenced by its yellow color (picture 1). However, the samples annealed in the H_2 (5%)/Ar environment exhibited a white color, indicating the reduction of Tb^{4+} ions from the material (pictures 2–4).

As the atmospheric pressure rises, the sample's color transitions from white to gray (picture 5) at 200 kPa, which may be attributable to the elevated argon pressure influencing the oxidation states of the Tb ions. This observation indicates that argon pressures may affect the valence state of the Tb ion, perhaps resulting in alterations to the material's optical characteristics. The light black color in white phosphor powder following high-pressure H_2 (5%)/Ar reduced atmosphere (200 kPa) annealing may be caused by oxygen vacancy growth, color centers, and other structural flaws that impact optical characteristics. The substance darkens, which usually causes luminescence loss. The band gap values (E_g) for the powdered materials were determined by the Kubelka–Munk (K–M) transformation using the diffuse reflectance spectra.[46] The determined band gap values for all the samples displayed slight variation, spanning from 5.4 eV to 5.5 eV, as shown in Fig. S1(a) and (b).

3.4. Diffuse reflectance infrared Fourier transform (DRIFT) spectroscopy

The DRIFT spectra of the $BaAl_2O_4$:Tb^{3+} (1 mol%) phosphor were recorded in the 4000–400 cm^{-1} range for samples annealed in air and H_2 (5%)/Ar atmospheres at different pressures. The spectra shown in Fig. 5(a) and (b) reveal that the bands around 413, 607, 667, 700, and 860 cm^{-1} are associated with Ba–O vibrations.[47,48] The bands at 436, 642, 813, and 909 cm^{-1} are attributed to Al–O vibrations.[31,47–49] The band at 1451 cm^{-1} is due to $BaCO_3$, while the asymmetric stretching vibration of CO_2 is observed at 2361 cm^{-1}.[48] The band at 3614 cm^{-1} corresponds to the O–H stretching vibration.[50] The sample annealed in argon at 60 kPa exhibits markedly enhanced Ba–O and Al–O vibrations relative to the other samples. Furthermore, except for the sample annealed in argon at 60 kPa, all other samples exhibit a shift in the Al–O band from 430 cm^{-1} to 436 cm^{-1}, signifying an increase of lattice energy vibrations and enhanced phonon activity. This shift indicates that the sample annealed in argon at 60 kPa has a more well-ordered crystal lattice, as

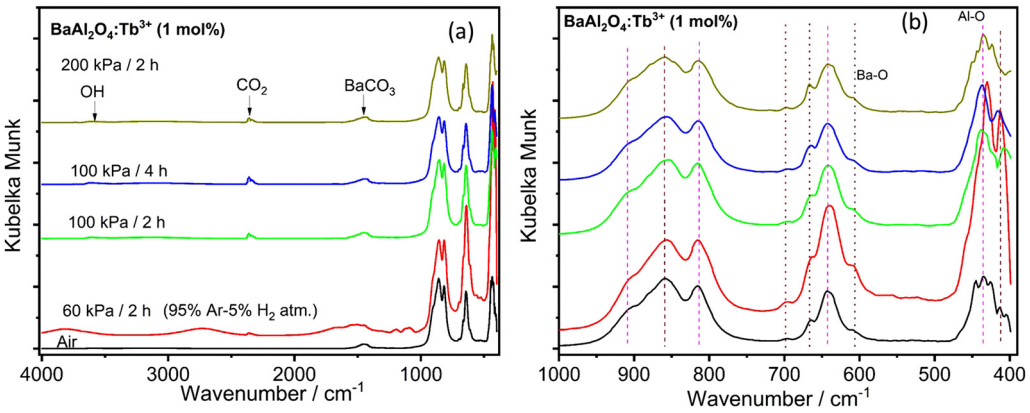

Fig. 5 (a) DRIFT spectra of $BaAl_2O_4$:Tb^{3+} (1 mol%) phosphor annealed in air and under different pressures of a reducing atmosphere (H_2 (5%)/Ar). (b) Magnified range (400–1000 cm^{-1}) of the DRIFT spectra for the $BaAl_2O_4$:Tb^{3+} (1 mol%) phosphor.

evidenced by the sharper and more distinct peaks due to fewer phonon vibrations. The vibrations of $BaCO_3$, CO_2, and OH show no change.

3.5. Surface chemical analysis

The XPS spectra of the Ba 3d region for materials annealed at 1200 °C in air and H_2 (5%)/Ar atmospheres are shown in Fig. 6(a) and (b). Each of the Ba $3d_{5/2}$ and Ba $3d_{3/2}$ peaks can be fitted into three components. The first two lower binding-energy peaks are separated by approximately 1.1 eV. These lower binding-energy peaks, located at 779.2 ± 0.1 eV and 780.3 ± 0.1 eV and denoted as Ba1 and Ba2, respectively, were assigned to Ba^{2+} ions occupying Ba1 and Ba2 sites in the $BaAl_2O_4$ hexagonal phase.[15,18] The higher binding-energy peak at 781.5 ± 0.3 eV is attributed to Ba atoms in a surface barium carbonate ($BaCO_3$) layer, consistent with previous reports.[15] The formation of a carbonate layer on the surface of $BaAl_2O_4$ has been previously documented and thus is expected to occur in the present case. Further support for the presence of $BaCO_3$ comes from FTIR analysis of $BaAl_2O_4$:Tb^{3+} materials, which exhibited a distinct absorption band at 1451 cm^{-1}, as shown in Fig. 5 (FTIR). It is worth noting that FTIR spectroscopy is recognized as one of the most sensitive techniques for detecting surface carbonate layers. The Ba $3d_{5/2}$ and Ba $3d_{3/2}$ peaks are separated by 15.3 eV.[51] The $BaCO_3$ component decreased from 23% to 12% after the material was annealed under a reducing atmosphere at a pressure of 60 kPa.

For the O 1s spectra of these materials, as shown in Fig. 6(c) and (d), five and four peaks were observed for materials annealed at 1200 °C in air and H_2 (5%)/Ar atmospheres, respectively. The fitted peak 1 (529.5 ± 0.1 eV) and peak 2 (530.6 ± 0.1 eV) correspond to lattice oxygen bonded to Ba and Al atoms at their regular crystallographic positions. Peak 3 (531.2 ± 0.1 eV) is attributed to oxygen atoms in surface $BaCO_3$. Peaks 4 (531.5 eV) and 5 (532.8 eV), observed in the air-annealed sample, are associated with interstitial oxygen and adsorbed water (H_2O).[30] In contrast, the material annealed under a H_2 (5%)/Ar atmosphere exhibited a peak at 532 eV corresponding to surface hydroxyl species (–OH). These findings are consistent with the thermoluminescence analysis. FTIR spectra further confirmed the presence of these surface impurities. The presence of water molecules at the surface lowers the intensity of PL by enhancing non-radiative processes *via* vibrational channels. In addition, dynamic interactions with polar water molecules induce broadening of the PL peak.[52,53] The broadening of the PLE spectra is evident in Fig. 7(a) (see the PL section).

The XPS spectrum of Tb 3d, shown in Fig. 6(e) and (f), exhibits three peaks centered at 1240 ± 0.2, 1241.1 ± 0.2, and 1242.5 eV. The lower binding-energy peaks (1240 ± 0.2, 1241.1 ± 0.2) were attributed to Tb^{3+} ions occupying the Ba1 and Ba2 sites within the lattice structure.[33] In contrast, the higher binding-energy peak at 1242.5 eV corresponded to the presence of Tb^{4+} ions in the sample annealed under an air atmosphere. Notably, the Tb^{4+} peak was absent in the material annealed under a reducing atmosphere of 60 kPa H_2 (5%)/Ar. This indicates that annealing the aluminate sample in reducing conditions prevents the oxidation of Tb ions at high temperatures. The UV-vis diffuse reflectance measurements support this result well. The reduction of $BaCO_3$ and Tb^{4+} ions resulted in improved luminescence intensity and quantum yield.

3.6. Photoluminescence

A key finding of this study was the influence of the annealing environment on the luminescence characteristics of the sample. A significant enhancement in PL intensity was observed when the annealing atmosphere was changed from air to 5% H_2/Ar at pressures between 60 and 100 kPa, as shown in Fig. 7. Fig. 7(a) shows the excitation spectra of $BaAl_2O_4$:Tb^{3+} (1 mol%) phosphor annealed in air and H_2 (5%)/Ar atmosphere, monitored at 547 nm emission. A wide band spanning from 200 to 300 nm, with a peak maximum of 228 nm (5.44 eV),[18] was detected, this band is associated with the $4f^8 \rightarrow 4f^75d^1$ band of Tb^{3+} with f–f transitions of Tb^{3+} observed between 300 and 500 nm.[54] All samples, except for the one annealed at 60 kPa, exhibited substantial broadening of the excited electronic states during photoluminescence excitation (PLE), which can be attributed to phonon-assisted scattering mechanisms.[55] In addition, the intensity of the $4f^8 \rightarrow 4f^75d^1$ transition band

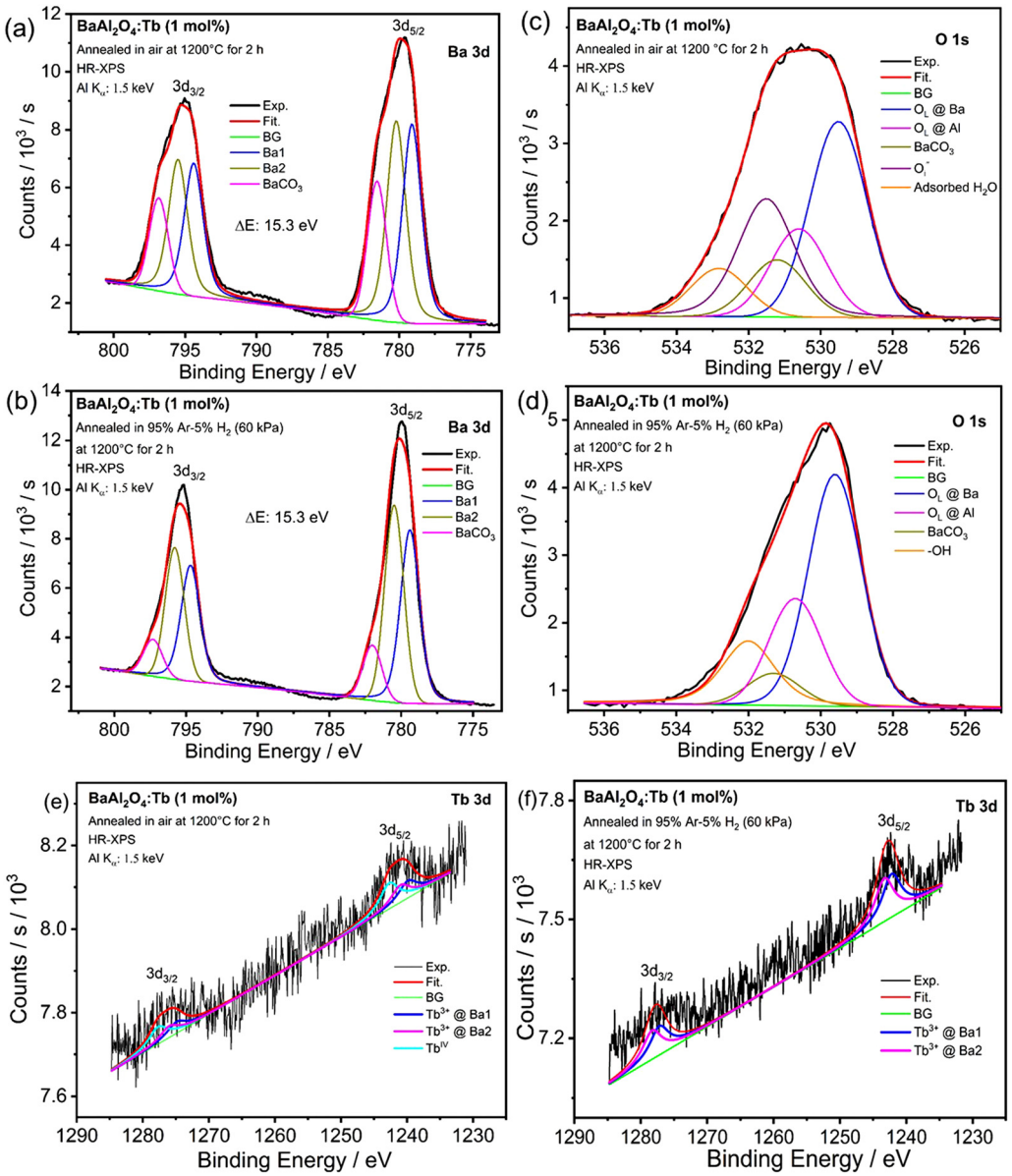

Fig. 6 XPS high resolution peaks for the Ba 3d (a) and (b), O 1s (c) and (d) and Tb 3d (e) and (f) ions in the $BaAl_2O_4$:Tb (1 mol%) phosphors annealed in air and 60 kPa pressure of H_2 (5%)/Ar reduced atmospheres.

of Tb^{3+} increased up to the sample annealed at 1200 °C for 2 h under a H_2 (5%)/Ar pressure of 100 kPa. Subsequently, it decreased with further increases in H_2 (5%)/Ar pressure during annealing. This suggests that the material annealed at 1200 °C for 2 h under a H_2 (5%)/Ar pressure of 100 kPa exhibits Tb^{3+} ions well accommodated at the Ba^{2+} sites within the $BaAl_2O_4$ lattice, with lattice parameters and unit cell volume closely matching the calculated values (see Table 1).

Fig. 7(b) shows the emission spectra of $BaAl_2O_4$:Tb^{3+} (1 mol%) samples upon excitation at 228 nm. The peaks observed in the range of 380–480 nm are attributed to the $^5D_3 \rightarrow {}^7F_J$ (J = 6, 5, and 4) transitions of Tb^{3+}, although these peaks are relatively weak in intensity due to cross-relaxation transition.[56] The four distinct emission bands were observed at 490, 544, 586, and 622 nm, which correspond to the $^5D_4 \rightarrow {}^7F_6$, $^7F_5$, $^7F_4$, and $^7F_3$ transitions of Tb^{3+} ions, respectively. The green emission intensity of the $^5D_4 \rightarrow {}^7F_5$ transition at 547 nm was higher than that of the other transitions in both the samples annealed in air and a H_2 (5%)/Ar environment.[57] Compared to the air-annealed sample, the samples annealed in a H_2 (5%)/Ar-reducing environment demonstrate improved luminescence intensity, attributed to greater Tb^{3+} ions (*i.e.*, reduction Tb^{4+} to Tb^{3+}). Due to the absorption of light by Tb^{4+} in the green-yellow wavelength range of the visible spectrum, the luminescence intensity is relatively low. However, when Tb^{4+} is reduced or fully converted to Tb^{3+}, the luminescence intensity increases significantly.[18] Furthermore, the material annealed at 1200 °C for 2 h under a H_2 (5%)/Ar pressure of 100 kPa exhibited strong

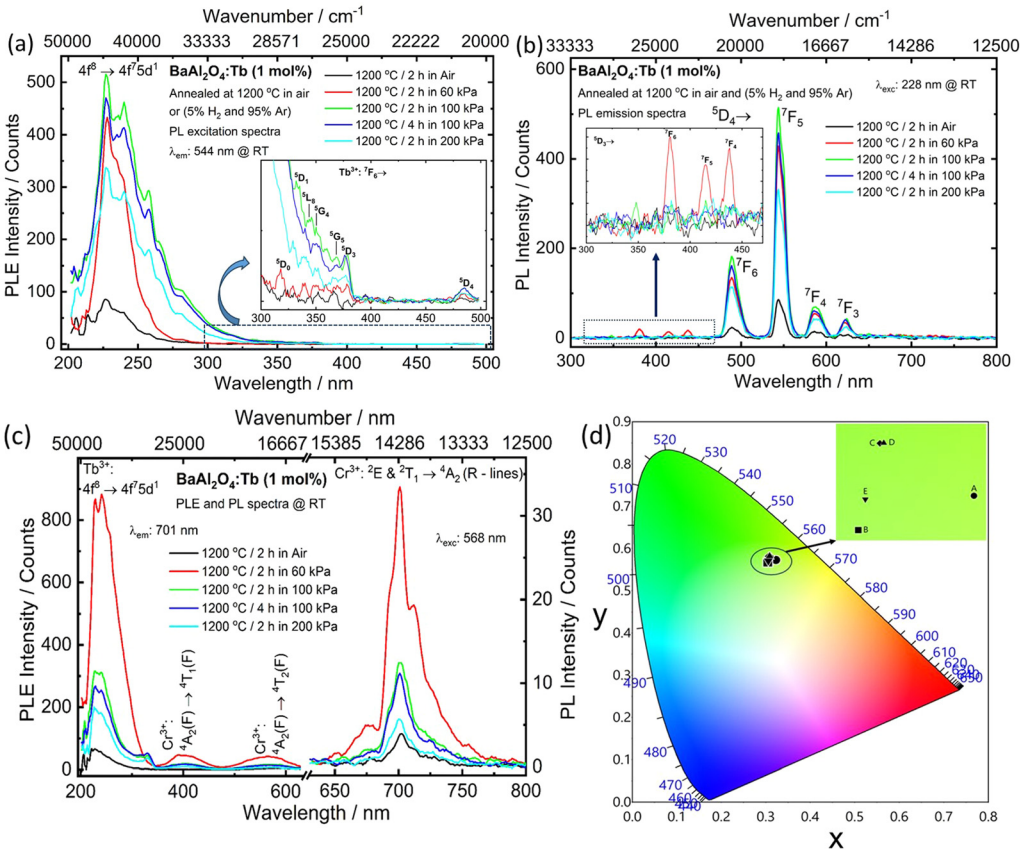

Fig. 7 (a) PL excitation spectra, (b) emission spectra, (c) both excitation and emission spectra and (d) CIE chromaticity diagram of $BaAl_2O_4$:Tb (1 mol%) phosphors annealed in air and selected pressures of a H_2 (5%)/Ar reduced atmosphere. The insets in (a) and (b) show the corresponding magnified excitation and emission spectra, respectively. The inset in (d) shows a magnified CIE chromaticity diagram (A, B, C, and D are represented as samples annealed in air, 2 h in 60 kPa, 2 h in100 kPa, 4 h in 100 kPa, and 2 h in 200 kPa, respectively).

blue, green, and red emissions corresponding to Tb^{3+} transitions, and these results were in good agreement with the PLE spectra.

Fig. 7(c) presents the PLE (λ_{em} = 701 nm) and PL (λ_{exc} = 568 nm) spectra of the Tb^{3+} singly activated $BaAl_2O_4$ samples. The PLE spectrum exhibits a prominent excitation band centered at 228 nm, attributed to the spin-allowed 4f → 5d transition of Tb^{3+} ions.[18] In addition, two weaker excitation bands centered at 400 nm and 568 nm were observed, which are ascribed to the spin-allowed transitions $^4A_{2g}$ (F) → $^4T_{1g}$ (F) and $^4A_{2g}$ (F) → $^4T_{2g}$ (F) of Cr^{3+} ions, respectively.[15,58] Under 580 nm excitation, the $BaAl_2O_4$:Tb^{3+} (1 mol%) samples exhibited a sharp emission at 701 nm, corresponding to the ^2E_g → $^4A_{2g}$ (R-line) transition of Cr^{3+} ions.[38] The presence of Cr^{3+} impurities in the $BaAl_2O_4$:Tb^{3+} (1 mol%) samples has been discussed in the UV-vis diffuse reflectance spectra section and previously published studies.[15,18] Fig. 7(d) shows the Commission International de L'Eclairage (CIE) chromaticity coordinates of the $BaAl_2O_4$:Tb^{3+} (1 mol%) samples based on their PL spectra (λ_{exc} = 228 nm) in Fig. 7(d). We found that the emission colors of these samples could be in the green region.

The PL decay curves were observed by measuring the emission at 543 nm, as illustrated in Fig. 8(a). These curves were most accurately represented by double-exponential functions, which were characterized by the following equation:

$$I(t) = I_0 + A_1 e^{-t/\tau_1} + A_2 e^{-t/\tau_2}$$

where $I(t)$ denotes the luminescence intensity at $t = t$, I_0 is the initial intensity at $t = 0$, τ_1 and τ_2 are the fast- and slow-decay components, respectively, and parameters A_1 and A_2 are fitting constants. The average decay time of the $^5D_4$ level of Tb^{3+} emission in $BaAl_2O_4$:Tb^{3+} (1 mol%) phosphor, annealed in both air and a reducing atmosphere at selected pressures (60 kPa for 2 h, 100 kPa for 2 h, 100 kPa for 4 h, and 200 kPa for 2 h), are 1.6, 2.0, 1.7, 1.6, and 1.6 ms, respectively (Fig. 8(b) and (c)). It can be observed that the phosphor annealed in the reducing atmosphere at 60 kPa exhibited the maximum lifetime of the $^5D_4$ level of Tb^{3+} emission. This implies that the absence of Tb^{4+} in the host lattice results in a more significant energy transfer (ET) from $4f^6$ → $4f^75d^1$ to the Tb^{3+} in the phosphor annealed in the reducing atmosphere at 60 kPa than the phosphor annealed in air, with a minimal amount of energy being absorbed by the lattice. Thus, the PL lifetime of the phosphor annealed at 60 kPa has increased by 25% compared to the phosphor annealed in air. The measured average lifetime of the $^5D_4$ level

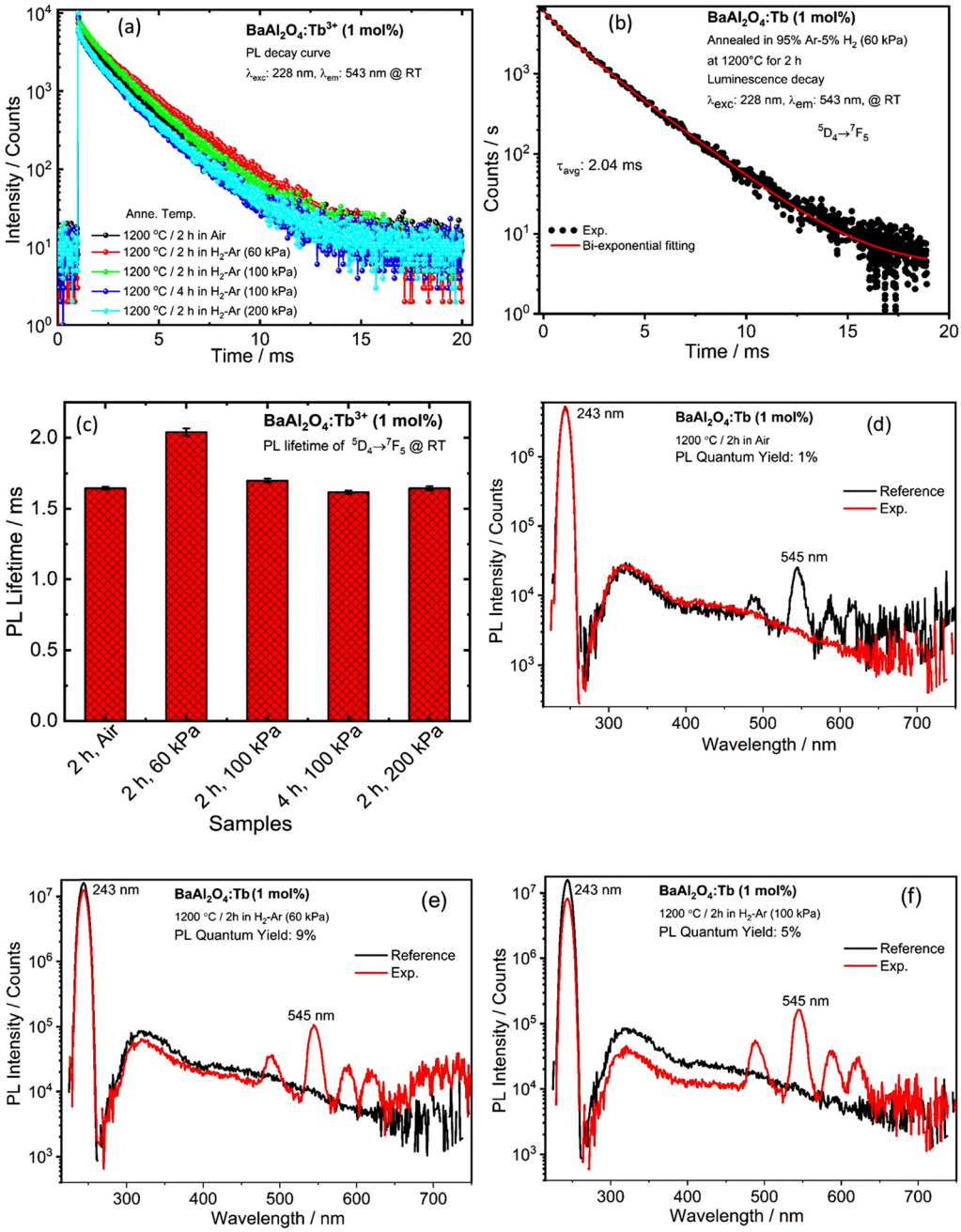

Fig. 8 (a) Room temperature PL decay curves, (b) fitted PL decay curve, and (c) variation graph of $BaAl_2O_4$:Tb (1 mol%) phosphors annealed in air and at selected pressures of a H_2 (5%)/Ar reduced atmosphere; PLQY measurement of $BaAl_2O_4$:Tb (1 mol%) phosphors annealed in air (d), and in selected pressures of a H_2 (5%)/Ar reduced atmosphere: (e) 60 kPa and (f) 100 kPa, with $BaSO_4$ as a reference, measured using an integrating sphere for internal quantum efficiency (IQE) determination.

of Tb^{3+} is well consistent with our previous report[18] and published literature.[59]

The photoluminescence quantum yield (PLQY) measurements for $BaAl_2O_4$:Tb (1 mol%) phosphors annealed in air and under selected pressures of a H_2 (5%)/Ar reduced atmosphere are shown in Fig. 8(d)–(f). These measurements used $BaSO_4$ as a reference and an integrating sphere under 243 nm excitation. Qualitatively, the internal quantum efficiency (IQY) represents the ratio of emitted and absorbed photons. The IQY value (ϕ) for $BaAl_2O_4$:Tb (1 mol%) phosphors can be estimated using the equations provided in ref. 60:

$$\phi = \frac{\int L_S}{\int E_R - \int E_S}$$

where, L_S represents the phosphor's emission spectrum, and E_S and E_R refer to the excitation light spectrum with and without the phosphor in the integrating sphere, respectively. The IQY values were found to be 1%, 9%, and 5% for

$BaAl_2O_4$:Tb (1 mol%) phosphors annealed in air, and at selected 60 kPa and 100 kPa pressures of a H_2 (5%)/Ar reduced atmosphere, respectively. Notably, the phosphor annealed at 60 kPa pressure in the H_2 (5%)/Ar reduced atmosphere exhibited the highest PLQY, significantly better than the phosphor annealed in air.

3.7. Electron paramagnetic resonance

The electron paramagnetic resonance (EPR) spectra of $BaAl_2O_4$:Tb phosphor annealed in air and reducing atmosphere were recorded at RT and are shown in Fig. 9. The EPR spectra contain several resonances in the 0–500 mT range, and an intense signal is observed at ~300 mT corresponding to g = 2.20. The satellite resonances are not symmetrically positioned relative to the intense signal at g = 2.20, and the separations between them are quite broad. This suggests that the satellites cannot be described solely by zero-field or hyperfine splitting.[61] The relatively weak satellites appear in the full range of magnetic field from 0 to 235 mT, corresponding to g = 19.37, 7.90, 5.65, and 4.32. The observed g-factors are attributed to the local symmetry between the dopant ions and the host lattice, such as tetrahedral or octahedral geometry. These g-factors play a crucial role in exploring the electronic configurations of rare-earth ions. In rare-earth systems, deviations of the g-values from the free electron value (2.0023) arise due to spin–orbit interactions influenced by the surrounding lattice environment.

EPR spectra of tetravalent terbium (Tb^{4+}) ions consist of broad resonances. The Tb^{4+} ions reveal results consistent with a $4f^7$ electronic configuration. Similar to Eu^{2+} and Gd^{3+}, Tb^{4+} belongs to a series of $4f^7$ ions, all possessing a half-filled $4f^7$ configuration with a ground state of $^8S_{7/2}$, characterized by zero orbital momentum (L = 0) and a spin value of S = 7/2. Consequently, they are expected to exhibit minor zero-field splitting (ZFS) parameters (which are typically $|D| < \sim 0.1$ cm^{-1}, where D is the axial, second-order ZFS) due to the absence of other octet states and the ground state octet is separated by a large energy gap from the first excited sextet state.[62]

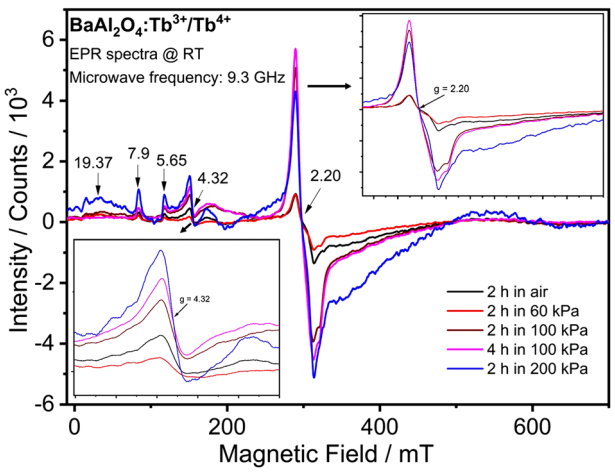

Fig. 9 EPR spectra of $BaAl_2O_4$:Tb (1 mol%) phosphors annealed in air and under selected pressures of a 5% H_2/Ar reduced atmosphere.

At room temperature, the EPR spectrum of $BaAl_2O_4$:Gd^{3+} displays resonance at g-factors of 2.14, 4.56, and 6.75. The signal at g = 2.14 is associated with Gd^{3+} ions occupying octahedral or tetrahedral symmetry sites with moderate distortion. At the same time, the resonance at g = 6.75 corresponds to a cubic crystal field environment with a moderate distortion.[63] The EPR spectra of the $xGd_2O_{3(1-x)}(Bi_2O_3–PbO)$ glass system reveal, at low Gd_2O_3 concentrations ($x \leq 0.05$), three characteristic absorption features at g = 2.0, 2.9, and 6.0. These features correspond to the well-known "U" spectrum, typical of Gd^{3+} ions in disordered polycrystalline environments. They are generally attributed to Gd^{3+} ions occupying sites with weak crystalline fields of varying symmetries—tetrahedral, octahedral, or distorted cubic—typically with coordination numbers greater than six.[64] The Eu^{2+} has 7 unpaired electrons ($4f^7$, S = 7/2), and the EPR signals that appeared are due to the Eu^{2+} ion. If Eu^{2+} ions occupy a high-symmetry site, they will display a strong EPR signal at g = 2. Additionally, due to their electron spin quantum number of 7/2, zero-field splitting may arise from electron–electron dipole interactions. This splitting seems to be symmetrically around the intense central resonance, based on the local symmetry around the Eu^{2+} ions.[65] Vijay Singh *et al.*[61] studied the EPR spectrum of $BaMgAl_{10}O_{17}$:Eu^{2+} phosphor and identified several resonance signals, of which the most intense peaks were at g = 4.63 (~150 mT). In a different study, the EPR spectrum of $BaAl_{12}O_{19}$:Eu,Mn phosphor exhibited a signal with a high intensity at $g \approx 4.81$, which was attributed to Eu^{2+} ions.[66]

Chromium ions (Cr^{3+}), with a $3d^3$ electronic configuration, exhibit a ground state of ^4F as predicted by Hund's rules. This term splits into an orbital singlet $^4A_{2g}$ and two orbital triplets, $^4T_{1g}$ and $^4T_{2g}$, due to crystal field effects in an octahedral crystal field environment. The EPR spectrum of Cr-doped $CaAl_{12}O_{19}$ phosphors in the low-field region displays multiple resonance signals at g = 5.59, 4.86, 4.13, 3.64, and 3.37, which are attributed to isolated Cr^{3+} ions occupying sites of varying local environments.[67] In the case of $BaAl_2O_4$:Cr phosphors, the EPR spectrum is characterized by a broad resonance at g = 4.93 and a sharp, intense resonance centered at g = 1.95. The low-field resonance at g = 4.93 is associated with isolated Cr^{3+} ions. At the same time, the intense signal at g = 1.95 indicates exchange-coupled Cr^{3+} ion pairs, likely arising from occupancy of strongly distorted or clustered sites.[9] Yiling Wu *et al.*[68] reported that EPR signals with g = 1.993 are observed exclusively in Cr^3-doped $La_3Ga_5GeO_{14}$, suggesting that these signals are associated with Cr^3-related trap centers. Mironova-Ulmane *et al.*[69] studied EPR resonances in the range of $g \approx$ 2–4, which arise from the substitution of Cr^{3+} ions for Al^{3+} sites in the spinel structure of $MgAl_2O_4$.

In the present study, the EPR spectra of $BaAl_2O_4$:Tb^{3+}/Tb^{4+} phosphor processed in both air and reducing atmospheres are in good agreement with the previously reported EPR spectrum of Tb^{4+} by Thaige P. Gompa *et al.*[62] Furthermore, the spectral profile and corresponding g-factors are consistent with those reported by Nakamura *et al.*[65] for Eu^{2+}-doped $BaAl_2O_4$, as well as with previously reported data on Eu^{2+}/Eu^{3+}-doped $BaAl_2O_4$

phosphors.[15] Also, the observed EPR resonances align well with characteristic *g*-factors reported for Gd^{3+} (ref. 63 and 64) and Cr^{3+} (ref. 9 and 67–69) ions. These results suggest that the EPR resonances observed at g = 19.37, 7.90, 5.65, and 4.32, and the intense signal at g = 2.20 can be attributed to Tb^{4+} ions occupying the Ba1 and Ba2 sites, which possess octahedral coordination in the hexagonal crystal structure of $BaAl_2O_4$. Some of these signals may also be attributed to Cr^{3+} impurities present in the tetrahedral coordination environment of AlO_4 surveyed units within the matrix. The results from UV-vis diffuse reflectance and PL spectroscopy support these findings well.

In the $BaAl_2O_4$ phosphor, the eightfold degenerate ground state splits into four Kramers doublets. The EPR spectrum should ideally show seven fine-structure lines due to intra- and inter-doublet transitions.[63] Additionally, spectral resonances at $g \gg 2.0$ and $g < 2.0$ are also observed. The resonance signal at a *g*-factor of 2.20 is attributed to paramagnetic ions located at sites with relatively weak ligand fields, where the Zeeman interaction dominates.[61] However, in this study, only a broad and poorly resolved spectral component was observed, which is attributed to enhanced dipolar interactions among neighboring Tb^{4+} ions.[64] Furthermore, the EPR spectrum of this phosphor shows contributions from both Tb^{4+} ions and clustered Cr^{3+} impurities, resulting in a broad and asymmetric absorption line centered at g = 2.20. In addition, the phosphor may contain a high density of Tb^{4+} and Cr^{3+} ions, which results in the EPR spectrum displaying a single broad absorption line centered at g = 2.20.[64]

The number of spins (N) participating in resonance at g = 2.20 and g = 4.32 at room temperature was calculated for $BaAl_2O_4$:Tb phosphors annealed in air and 5% H_2/Ar atmospheres. The estimated N values are accessible in Table S1. The sample treated at 60 kPa for 2 hours in 5% H_2/Ar exhibited the lowest number of spins participating in resonance at g = 2.20 and g = 4.32, indicating a reduced concentration of Tb^{4+} ions, fewer oxygen vacancies, and minimal distortion around the rare-earth ions because of the heat treatment under these conditions. Takeru Kinoshita *et al.*[70] reported that the Tb^{3+}-activated reduced calcium aluminate glasses exhibited a symmetric EPR signal at g = 1.999. This signal is attributed to an electron trapped at an oxygen vacancy site coordinated by Ca^{2+} ions, forming an F^+-center in the CaO environment.[70] However, the $BaAl_2O_4$:Tb phosphors contain oxygen vacancies when processed under a reducing environment, contributing to the resonance signal at g = 2.20, resulting in a broad absorption feature. The broadening and asymmetry of this signal can also be attributed to interactions with nearby paramagnetic ions.[71] At higher annealing pressures in a 5% H_2/Ar atmosphere, the population of spin levels at g = 2.20 and g = 4.32 increased, as observed in the EPR spectra. This shows higher oxygen vacancy concentration, and other color centers formed due to highly reduced conditions.[72,73] Therefore, the color of phosphor powder changed from white to light black. At a still greater reduction pressure (200 kPa), the sample was determined to be of darker black color. This growth in defects is also apparent from a drop in the diffuse reflectance spectra. The same observation was reported by Li-Wu Zhang *et al.*[73] for the $BaAl_2O_4$ powdered processed under a H_2 atmosphere. These findings and the data of Table S1, indicate that enhanced reducing conditions strengthen the formation of a large density of oxygen vacancies and accompanying lattice distortions in $BaAl_2O_4$:Tb phosphors.

3.8. Thermoluminescence

The intensity, position, and shape of the glow curves of the TL in $BaAl_2O_4$:Tb are strongly affected by the processing atmosphere, as shown in Fig. 10(a). The $BaAl_2O_4$:Tb phosphor annealed at 1200 °C for 4 h in a H_2 (5%)/Ar atmosphere was found to be the most efficient in TL and, therefore, in energy storage. This indicates that the characteristics of the traps involved in energy storage are influenced by the preparation atmosphere. The glow curves were normalized to the same height (see Fig. S2). The TL glow curves were found to consist of a broad band with a maximum at approximately 61 °C and 139 °C, and a broad band with a peak at 365 °C, which were identified as T_{m_1}, T_{m_2}, and T_{m_3} in Fig. S2. The peak position of the high-temperature peak, T_{m_3}, shifts, and its corresponding FWHM increases compared to that of the phosphor annealed in air. This confirms that the phosphor processed in the H_2 (5%)/Ar atmosphere for T_{m_3} consists of two peaks attributed to two traps located at different depths in the material. These peaks can be attributed to the presence of oxygen vacancies, which act as electron or hole traps (or both) within the energy gap of the host material. These relatively shallow traps are responsible for storing energy for a short duration, contributing to persistent luminescence. In contrast, deeper traps store energy for longer and are suitable for photostimulated luminescence and radiation dosimetry.

As a function of the processing atmosphere, the TL intensities of T_{m_1}, T_{m_2}, and T_{m_3} increase with the increase in H_2 (5%)/Ar Ar atmospheric pressure up to 100 kPa for an annealing time of 4 h. However, with further increases in the H_2 (5%)/Ar atmospheric pressure, the intensities of these peaks decrease, as shown in Fig. 10(a). The peak intensity of TL is affected by various parameters, such as material geometry and surface area. The dimensions and configuration of the material, along with the surface area exposed to radiation, might influence the quantity of trapped charge carriers, thus impacting the TL intensity. A secondary component is the existence and efficacy of recombination centers, including impurities or defects. These centers are crucial to the TL process, and misalignment with the trapped charges can diminish the efficacy of thermoluminescence. The third component pertains to material imperfections consisting of vacancies, dislocations, or impurities. These faults can generate supplementary trapping sites or recombination centers, modifying the TL properties and peak intensity.[74,75] $BaAl_2O_4$:Tb phosphors annealed in air and under the lowest H_2 (5%)/Ar atmospheric pressure content (60 kPa) exhibited the lowest TL intensity, while those annealed with 100 kPa and 200 kPa samples show higher TL signals. This confirms that a higher H_2 (5%)/Ar content in the annealing atmosphere shows maximum TL intensity. These findings

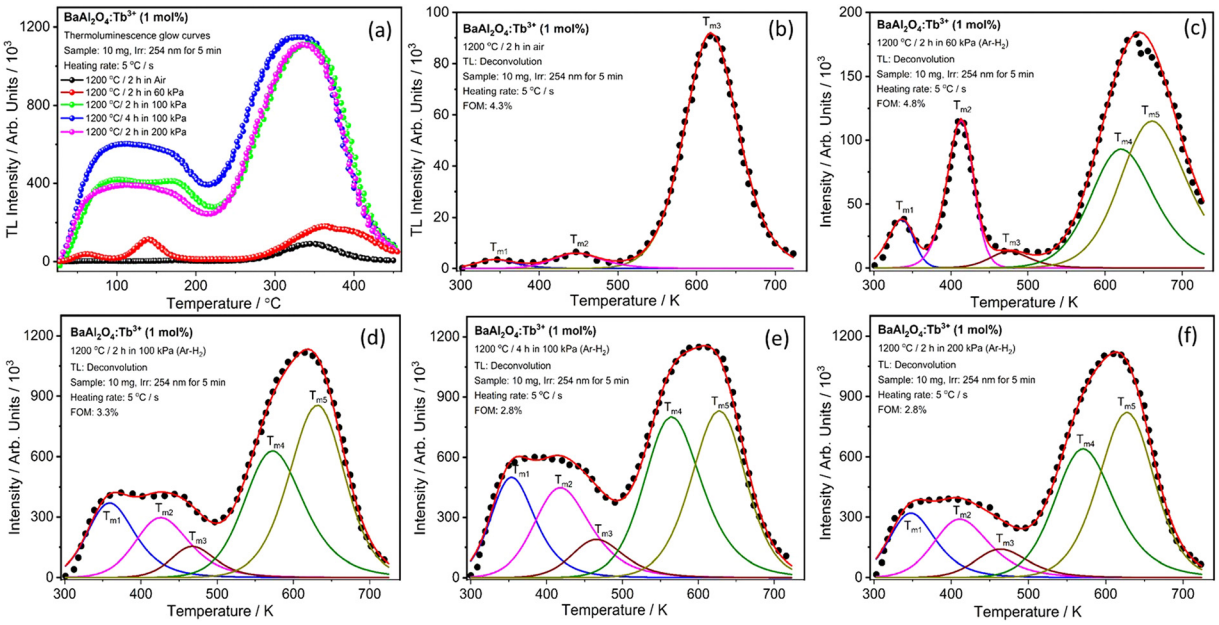

Fig. 10 Thermoluminescence (TL) glow curves (a) and deconvoluted TL glow curves (b)–(f) of UV (254 nm)-irradiated $BaAl_2O_4$:Tb (1 mol%) phosphors annealed in air and at selected pressures of a H_2 (5%)/Ar reduced atmosphere.

indicate that trapping defects involved in TL are directly linked to the oxygen content in the crystal. Specifically, they are associated with oxygen deficiency in the material: the lower the oxygen concentration in the annealing atmosphere, the more intense the TL. These results provide compelling evidence for the role of oxygen vacancies in the material's TL properties. Samuel Blahuta *et al.*[75] reported on the effects of annealing on $Lu_2Y_2SiO_5$ single crystals for scintillation applications, finding that air annealing at 1500 °C effectively reduced TL intensity, corresponding to a decrease in oxygen vacancies. In contrast, annealing in a reducing atmosphere led to the opposite effect, increasing TL intensity.

When the material is annealed in air, a surface reaction with atmospheric oxygen can occur. One possible mechanism involves oxygen adsorption through its interaction with Tb^{3+} impurities, which are associated with the TL behavior of the aluminate. This reaction leads to the formation of O^{2-} ions, as represented by the following equation:

$$4Tb^{3+} + O_2 \rightarrow 4Tb^{4+} + 2O^{2-}$$

The O^{2-} center created near the surface acts as an electron trap, as the annealing in air.

In a H_2 (5%)/Ar atmosphere, hydrogen acts as a reducing agent, facilitating the reduction of Tb^{4+} to Tb^{3+}. The reduction of Tb^{4+} to Tb^{3+} in a H_2 (5%)/Ar atmosphere can be represented by the following equation:

$$Tb^{4+} + \frac{1}{2}H_2 \rightarrow Tb^{3+} + H^+$$

In this process, increasing the H_2 (5%)/Ar content leads to more oxygen deficiencies. As a result, a new TL peak emerges, and the TL signal becomes larger at H_2 (5%)/Ar atmospheric pressure up to 100 kPa, with an annealing time of 4 h. At a high annealing pressure of H_2 (5%)/Ar (200 kPa), the TL signal is reduced due to the formation of a high density of oxygen vacancies and other structural defects that affect the material's TL properties. These defects aggregate into centers that diminish the number of recombination centers, thereby decreasing the energy transfer from recombination centers to emitter centers.

These findings agree with the results from UV-vis diffuse reflectance and PL spectroscopy.

The TL glow curves were fitted using the equations provided by Kitis *et al.*[76] The material processed in air exhibited three TL peaks attributed to two $\left[Tb^{3+}\right]^{\bullet}_{Ba}$ electron traps and an O_i'' hole trap. These traps were identified and reported in our previous work, where $BaAl_2O_4:Tb^{3+}$ was synthesized using solution combustion synthesis and subsequently annealed in air at 1100 °C. In contrast, the material processed in a H_2 (5%)/Ar atmosphere at various pressures displayed five TL peaks. The additional two peaks (T_{m_3} and T_{m_4}) are likely associated with oxygen vacancies. For the sample processed at 60 kPa in the H_2 (5%)/Ar gas mixture, the TL peaks T_{m_4} and T_{m_5} shifted to higher temperatures, indicating that the corresponding trap depths were deeper. Each peak was fitted with first- and second-order kinetic equations to determine the most suitable model. The higher-temperature TL peaks (T_{m_5}) were found to follow first-order kinetics in the sample processed in air. In contrast, the sample processed in H_2 (5%)/Ar at a pressure of 60 kPa shows low-temperature TL peaks (T_{m_1} and T_{m_2}) that exhibit first-order kinetics. However, the samples processed at high pressure ($\geq$100 kPa) display second-order kinetics (see Table 2). This was also demonstrated in a previous study,[18] where the high-temperature TL peak exhibited first-order kinetics, whereas the

Table 2 TL kinetics parameters of UV radiation irradiated $BaAl_2O_4$:Tb^{3+} (1 mol%)

Sample	TL peaks	Peak temperature/K	Peak intensity/Arb. units/10^3	Trap depth, E/eV	Order of kinetics, b	FOM/%
Air	T_{m_1}	343	3.5	0.55	2	4.8
	T_{m_2}	444	6.0	0.85	1.8	
	T_{m_5}	618	91	1.15	1.5	
60 kPa	T_{m_1}	336	38	0.65	1.3	4.0
	T_{m_2}	413	116	1.0	1.4	
	T_{m_3}	475	13	1.05	2	
	T_{m_4}	620	93	1.1	2	
	T_{m_5}	660	115	1.2	2	
100 kPa/2 h	T_{m_1}	358	370	0.48	2	3.2
	T_{m_2}	425	297	0.6	2	
	T_{m_3}	467	154	0.9	2	
	T_{m_4}	572	629	1.0	2	
	T_{m_5}	631	855	1.15	1.55	
100 kPa/4 h	T_{m_1}	353	500	0.5	2	2.7
	T_{m_2}	417	448	0.55	2	
	T_{m_3}	465	190	0.75	2	
	T_{m_4}	564	800	1	2	
	T_{m_5}	627	830	1.15	1.55	
200 kPa/2 h	T_{m_1}	347	320	0.47	2	2.7
	T_{m_2}	410	290	0.55	2	
	T_{m_3}	463	141	0.75	2	
	T_{m_4}	570	640	1	2	
	T_{m_5}	627	820	1.15	1.55	

low-temperature TL peaks exhibited second-order kinetics for $BaAl_2O_4$:Tb phosphors prepared by solution combustion and annealed at 1100 °C for 2 hours in air after being irradiated with 10 min of UV (254 nm) radiation.

The calculated TL trapping parameters for the $BaAl_2O_4$:1 mol% Tb phosphor are summarized in Table 2, indicating that the phosphor trap depth increases with temperature. The traps depth (activation energy) varied from 0.48 to 1.2 eV, suggesting that these peaks correspond to traps located at shallow and deeper levels within the band gap of the phosphor. This illustrates the trapping of electrons in shallow trap centers, which contribute to persistent luminescence and influence the characteristics of PL at RT. In contrast, deeper traps contribute to the characteristics of TL dosimetry. The figure of merit (FOM), an essential parameter for assessing the performance and accuracy of the fit between experimental and theoretical data, was found to be less than 5%. This indicates that the fit was successful and that the deconvoluted peaks within the glow curve were accurately fitted, as shown in Fig. 10(b)–(f). These results demonstrate that the experimental and theoretical TL glow curves are in good agreement and closely overlap.

4. Conclusions

The green emission of Tb^{3+}-doped $BaAl_2O_4$ phosphors was enhanced through co-precipitation synthesis with annealing in a H_2 (5%)/Ar reducing atmosphere at 60 kPa. It eliminated the Tb^{4+} ions, diminishing non-radiative transitions and enhancing photoluminescence quantum efficiency from 1% to 9% under 243 nm excitation. The substitution of Tb^{3+} ions into Ba^{2+} sites leads to the creation of interstitial oxide ions in $BaAl_2O_4$ for charge compensation, confirmed by XPS analysis, resulting in strong green emission at 228 nm excitation. The reducing atmosphere also extended the $^5D_4$ state luminescence lifetime to approximately 2 ms, attributed to the absence of Tb^{4+} ions. EPR investigation confirms the presence of paramagnetic Tb^{4+} and Cr^{3+} ions in $BaAl_2O_4$:Tb. Additionally, a low concentration of oxygen vacancies was observed at 60 kPa, illustrating the impact of reducing atmosphere on defect formation. The thermoluminescence $BaAl_2O_4$:Tb annealed in air exhibited three trap states (0.55–1.15 eV), and the material annealed at a reducing atmosphere showed five trap states (0.5–1.2 eV), as confirmed by the thermoluminescence result. Furthermore, the low-temperature TL peaks (T_{m_1} and T_{m_2}) exhibited well-resolved and symmetrical profiles, characteristic of first-order kinetic behavior. The inhibition of Tb^{4+} formation by the reducing atmosphere ensures reproducible performance, and the scalable co-precipitation synthesis is conducive to industrialization. $BaAl_2O_4$:Tb^{3+} phosphor can be used as a promising material for several photonic and optoelectronic applications, primarily due to its strong green luminescence and potential persistent luminescence properties. It may be used in emergency and safety signage, solid-state lighting LEDs, optical markers or sensors, and with appropriate trap engineering, $BaAl_2O_4$:Tb^{3+} can exhibit long afterglow, suitable for low-level illumination without continuous power, such as path indicators or watch dials.

Author contributions

Divya Janardhana: investigation: materials' preparation, structural characterization, spectroscopic measurements; software;

thermoluminescence; visualization; writing – original draft, Shivaramu Nagarasanakote Jayaramu: investigation: structural characterization, spectroscopic analysis; software; thermoluminescence; visualization; writing – original draft, David E. Motaung: electron paramagnetic resonance measurements and interpretation and review & editing, Elizabeth Coetsee: X-ray photoelectron spectroscopy measurements and interpretation and review & editing, Hendrik C. Swart: supervision, conceptualization, funding acquisition, methodology, project administration, resources, supervision, writing – review & editing.

Conflicts of interest

There are no conflicts to declare.

Data availability

The data that support the findings of this study are available in the main text, SI, and from the corresponding authors upon request. Room temperature optical bandgap plot and variation graph for the $BaAl_2O_4$:Tb (1 mol%) phosphors annealed in air and selected pressures of an Ar-H_2 reduced atmosphere; Normalized thermoluminescence glow curves of UV (254 nm)-irradiated $BaAl_2O_4$:Tb (1 mol%) phosphors annealed in air and at selected pressures of a H_2 (5%)/Ar reduced atmosphere; estimated number of spins (N) participating in resonance at g = 2.20 and g = 4.32 at room temperature, extracted from EPR spectroscopy of powder samples, is provided in the table. See DOI: **https://doi.org/10.1039/d5ma00747j**

Acknowledgements

The authors express their sincere thanks to the South African Research Chairs Initiative of the Department of Science and Technology and the National Research Foundation of South Africa (No. 84415). The financial assistance from the University of the Free State is gratefully acknowledged.

References

1 D. Jia, X. J. Wang, E. Van Der Kolk and W. M. Yen, Site dependent thermoluminescence of long persistent phosphorescence of $BaAl_2O_4$:Ce^{3+}, *Opt. Commun.*, 2022, **204**(1–6), 247–251.
2 D. Sun, X. Zeng, Y. Fu, C. Miao, Z. Xiong and L. Yu, Luminescent color modulation of Zn/$BaAl_2O_4$:0.2%Eu phosphors for LED application, *Opt. Mater.*, 2024, **157**(P1), 116184.
3 X. Yin, Y. Tian, J. Chen, X. Yi, R. Jiang, D. Zhang, H. Lin, S. Zhou and S. Bai, Photoluminescence performance of $BaAl_2O_4$:Eu2+ cyan phosphor ceramics, *J. Appl. Phys.*, 2023, **133**(17), 175105.
4 R. W. Hyland, Jr., J. P. Quintenz, B. T. Dunville and G. Subrahmanyam, *US Pat.*, US 6969475 B2, 2005, **2**(12).
5 A. A. Setlur, R. G. Chandran, C. S. Henderson, P. K. Nammalwar and E. Radkov, *US Pat.*, US20100096974 A1, 2010.
6 Z. Xia and A. Meijerink, Ce^{3+}-Doped garnet phosphors: Composition modification, luminescence properties and applications, *Chem. Soc. Rev.*, 2017, **46**(1), 275–299.
7 Savita, A. Vij and A. Thakur, Luminescence study of alkaline earth aluminate-based nanophosphors, in *Radiat. Dosim. Phosphors*, ed. H. S. Sanjay Dhoble, V. Chopra, V. Nayar, G. Kitis and D. Poelman, Elsevier, 2022, pp. 327–355.
8 S. Benourdja, Ü. H. Kaynar, M. Ayvacikli, Y. Karabulut, J. G. Guinea, A. Canimoglu, L. Chahed and N. Can, Preparation and cathodoluminescence characteristics of rare earth activated $BaAl_2O_4$ phosphors, *Appl. Radiat. Isot.*, 2018, **139**, 34–39.
9 V. Singh, R. P. S. Chakradhar, J. L. Rao and J. J. Zhu, Studies on red-emitting Cr^{3+} doped barium aluminate phosphor obtained by combustion process, *Mater. Chem. Phys.*, 2008, **111**(1), 143–148.
10 Y. Kumari, L. K. Jangir, A. Kumar, M. Kumar and K. Awasthi, Luminescent and structural behaviour of Tb^{3+} ions doped TiO_2 nanoparticles synthesized by facile sol-gel method, *Phys. B*, 2021, **602**, 412465.
11 S. Liao, X. Ji, Y. Liu and J. Zhang, Highly Efficient and Thermally Stable Blue-Green (Ba0.8Eu0.2O)(Al2O3)-4.575×(1+x) Phosphor through Structural Modification, *ACS Appl. Mater. Interfaces*, 2018, **10**(45), 39064–39073.
12 Y. Tian, J. Chen, X. Yi, D. Zhao, Z. Weng, Y. Tang, H. Lin and S. Zhou, A new $BaAl_2O_4$-YAG: Ce composite ceramic phosphor for white LEDs and LDs lighting, *J. Eur. Ceram. Soc.*, 2021, **41**(7), 4343–4348.
13 A. Muley, S. B. Dhoble, P. Ramesh, R. S. Yadav and S. J. Dhoble, Recent development of aluminate materials for solid state lighting, *Prog. Solid State Chem.*, 2022, **66**, 100347.
14 D. Poelman, D. Van Der Heggen, J. Du, E. Cosaert and P. F. Smet, Persistent phosphors for the future: Fit for the right application, *J. Appl. Phys.*, 2020, **128**, 240903.
15 S. Nagarasanakote Jayaramu, D. Janardhana, L. J. B. B. Erasmus, E. Coetsee, D. E. Motaung and H. C. Swart, Influence of annealing temperature on persistent luminescence in $BaAl_2O_4$:Eu^{2+}/Eu3+ nanocrystals and its application for latent fingerprint detection, *Dalton Trans.*, 2024, **53**(40), 16557–16576.
16 X. Kang, S. Lu, H. Wang, D. Ling and W. Lü, Tricolor- and white light-emitting Ce^{3+}/Tb^{3+}/Mn^{2+}-coactivated $Li_2Ca_4Si_4O_{13}$ phosphor via energy transfer, *ACS Omega*, 2018, **3**, 16714–16720.
17 R. Chatterjee, G. C. Das and K. K. Chattopadhyay, Synthesis and characterization of highly luminescent green emitting $BaAl_2O_4$: Tb^{3+} nanophosphors, *Mater. Today: Proc.*, 2019, **18**, 1132–1137.
18 S. N. Jayaramu, E. Coetsee, J. Hölsä and H. C. Swart, Energy trapping to substitutional and charge compensation defects in persistent luminescent $BaAl_2O_4$:Tb^{3+}, *Phys. Scr.*, 2024, **99**(11), 115975.

19 D. A. Hakeem, Y. Kim and K. Park, Luminescent Characteristics of $Ba_{1-x}Al_2Si_2O_8$:xTb^{3+} Green Phosphors, *J. Nanosci. Nanotechnol.*, 2016, **16**(2), 1761–1764.
20 Y. Wang, P. Darapaneni, O. Kizilkaya and J. A. Dorman, Role of Ce in Manipulating the Photoluminescence of Tb Doped $Y_2Zr_2O_7$, *Inorg. Chem.*, 2020, **59**(4), 2358–2366.
21 C. Zhang, J. Qi, L. Liang, Y. Yan and T. Lu, Decolorization, spectral broadening, and luminescence enhancement in Tb:Y_2O_3 transparent ceramics through vacuum thermal reduction, *Opt. Lett.*, 2024, **49**(7), 1652.
22 A. V. Myshkina, I. N. Bazhukova, V. A. Pustovarov and S. Y. Sokovnin, Luminescent-optical properties of cerium dioxide nanoparticles annealed in a reducing atmosphere, *AIP Conf. Proc.*, 2019, **2174**, 020141.
23 N. J. Shivaramu, B. N. Lakshminarasappa, E. Coetsee and H. C. Swart, Thermoluminescent materials for high-energy dosimetry, *Radiat. Dosim. Phosphors*, Elsevier, 2022, pp. 211–251.
24 J. Du, X. Wang, S. Sun, Y. Wu, K. Jiang, S. Li and H. Lin, Pushing Trap-Controlled Persistent Luminescence Materials toward Multi-Responsive Smart Platforms: Recent Advances, Mechanism, and Frontier Applications, *Adv. Mater.*, 2024, **36**, 2314083.
25 L. C. V. Rodrigues, R. Stefani, H. F. Brito, M. C. F. C. Felinto, J. Hls, M. Lastusaari, T. Laamanen and M. Malkamki, Thermoluminescence and synchrotron radiation studies on the persistent luminescence of $BaAl_2O_4$:Eu^{2+},Dy^{3+}, *J. Solid State Chem.*, 2010, **183**(10), 2365–2371.
26 M. C. Manaka, B. M. Mothudi and M. S. Dhlamini, Photoluminescence and thermoluminescence properties of manganese doped $BaAl_2O_4$ phosphor, *Mater. Sci. Eng. B*, 2022, **278**, 115604.
27 J. Du and D. Poelman, Identifying near-infrared persistent luminescence in Cr^{3+}-doped magnesium gallogermanates featuring afterglow emission at extremely low temperature, *Adv. Opt. Mater.*, 2020, **8**, 1901848.
28 R. Chen and S. W. S. McKeever, *Theory of Thermoluminescence and Related Phenomena*, World Scientific, Singapore, 1997.
29 A. J. J. Bos, Theory of thermoluminescence, *Radiat. Meas.*, 2006, **41**, 45–56.
30 B. Cheng, L. Fang, Z. Zhang, Y. Xiao and S. Lei, $BaAl_2O4:Eu^{2+}$,Dy3+ nanotube synthesis by heating conversion of homogeneous coprecipitates and afterglow characteristics, *J. Phys. Chem. C*, 2011, **115**, 1708–1713.
31 Z. Zhu, X. Li, H. Li, Y. Li, C. Sun and Y. Cao, Synthesis and characterization of $BaAl_2O_4$ nanorods by a facile solvothermal method, *Mater. Lett.*, 2012, **86**, 1–4.
32 M. T. Spicher, S. P. Schwaminger, D. von der Haar-Leistl, M. M. Peralta, G. Mikacevic, F. E. Wagner and S. Berensmeier, Pilot-scale co-precipitation synthesis of a novel active ingredient made of ultrasmall iron (oxyhydr)-oxide nanoparticles for the treatment of hyperphosphatemia, *RSC Adv.*, 2024, **14**, 16117–16127.
33 A. Daigle, E. DuPre', A. Geiler, Y. Chen, P. V. Parimi, C. Vittoria and V. G. Harris, Preparation and characterization of pure-phase Co_2Y ferrite powders *via* a scalable aqueous coprecipitation method, *J. Am. Ceram. Soc.*, 2010, **93**, 2994–2997.
34 J. Divya, N. J. Shivaramu, W. Purcell, W. D. Roos and H. C. Swart, Effects of annealing temperature on the crystal structure, optical and photocatalytic properties of Bi_2O_3 needles, *Appl. Surf. Sci.*, 2020, **520**, 146294.
35 V. Ţucureanu, C. Romaniţan, I. A. Tudor, C. Ţucureanu, M. A. Popescu and A. Matei, Effect of process parameters on YAG:Ce phosphor properties obtained by co-precipitation method, *Ceram. Int.*, 2020, **46**(15), 23802–23812.
36 A. Bhargava, I. D. R. Mackinnon, T. Yamashita and D. Page, Bulk manufacture of YBCO powders by coprecipitation, *Phys. C*, 1995, **241**, 53–62.
37 F. Ji, S. Xiao, J. Cheng, D. Li, J. Liao, Y. Guo, H. Zhang, S. Zhang, Y. Wei, Y. Liu, N. Ci, Q. Gao, J. Wang and L. Ci, Low-cost and facile synthesis of LAGP solid state electrolyte via a co-precipitation method, *Appl. Phys. Lett.*, 2022, **121**, 023904.
38 W. Hörkner, H. Müller-Buschbaum, V. W. Horkner and H. Muller-Buschbaum, Zur Kristallstruktur von $BaAl_2O_4$, ZAAC, *J. Inorg. Gen. Chem.*, 1979, **451**(1), 40–44.
39 M. Zhao, Z. Xia, X. Huang, L. Ning, R. Gautier, M. S. Molokeev, Y. Zhou, Y. C. Chuang, Q. Zhang, Q. Liu and K. R. Poeppelmeier, Li substituent tuning of LED phosphors with enhanced efficiency, tunable photoluminescence, and improved thermal stability, *Sci. Adv.*, 2019, **5**, 1–7.
40 R. D. Shannon, Revised Effective Ionic Radii and Systematic Studies of Interatomie Distances in Halides and Chaleogenides, *Acta Crystallogr., Sect. A*, 1976, **32**, 751–767.
41 B. S. Yilbas, H. Ali, N. Al-Aqeeli, M. M. Khaled, S. Said, N. Abu-Dheir, N. Merah, K. Youcef-Toumi and K. K. Varanasi, Characterization of Environmental Dust in the Dammam Area and Mud After-Effects on Bisphenol-A Polycarbonate Sheets, *Sci. Rep.*, 2016, **6**(1), 24308.
42 V. Vitola, D. Millers, K. Smits, I. Bite and A. Zolotarjovs, The search for defects in undoped $SrAl_2O_4$ material, *Opt. Mater.*, 2019, **87**, 48–52.
43 L. C. V. Rodrigues, H. F. Brito, J. Ho, R. Stefani, M. C. F. C. Felinto, M. Lastusaari, T. Laamanen and L. A. O. Nunes, Discovery of the Persistent Luminescence Mechanism of $CdSiO_3$:Tb^{3+}, *J. Phys. Chem. C*, 2012, **116**, 11232–11240.
44 V. De Luz, M. Prades, H. Beltrán and E. Cordoncillo, Environmental-friendly yellow pigment based on Tb and M (M = Ca or Ba), *J. Eur. Ceram. Soc.*, 2013, **33**(15–16), 3359–3368.
45 Y. Kagamitani, D. A. Pawlak, H. Sato, A. Yoshikawa, H. Machida and T. Fukuda, Annealing Effect in Terbium–Scandium–Aluminum Garnet Single Crystal, *Jpn. J. Appl. Phys.*, 2002, **41**(Part 1, No. 10), 6020–6022.
46 U. Mushtaq, I. Ayoub, M. Y. A. Yagoub, N. J. Shivaramu, E. Coetsee, H. C. Swart and V. Kumar, Effect of Li^+ monovalent ion on the structural and optical properties of Dy^{3+} doped $ZnGa_2O_4$ phosphor, *Appl. Phys. A: Mater. Sci. Process.*, 2024, **130**(7), 494.
47 C. M. B. Henderson and D. Taylor, The structural behaviour of the nepheline family: (1) Sr and Ba aluminates ($MA1_2O_4$), *Mineral. Mag.*, 1982, **45**, 111–127.

48 U. Rodehorst, M. A. Carpenter, S. Marion and C. M. B. Henderson, Structural phase transitions and mixing behaviour of the Ba-aluminate ($BaAl_2O_4$)–Sr-aluminate ($SrAl_2O_4$) solid solution, *Mineral. Mag.*, 2003, **67**, 989–1013.

49 S. Wang, H. Gao, L. Fang, Y. Wei, Y. Li and L. Lei, Synthesis and Characterization of $BaAl_2O_4$ Catalyst and its Photocatalytic Activity Towards Degradation of Methylene Blue Dye, *Z. Phys. Chem.*, 2019, **233**, 1161–1181.

50 B. G. Zhai, Q. L. Ma, R. Xiong, X. Li and Y. M. Huang, Blue-green afterglow of $BaAl_2O_4$:Dy^{3+} phosphors, *Mater. Res. Bull.*, 2016, **75**, 1–6.

51 J. F. Moulder, W. F. Stickle, P. E. Sobol and K. D. Bomben, Handbook of X-ray Photoelectron Spectroscopy Edited by, Google Sch., 1993, pp. 1–261.

52 J. Yang, H. Fang and Y. Gao, Effect of Water Adsorption on the Photoluminescence of Silicon Quantum Dots, *J. Phys. Chem. Lett.*, 2016, **7**(10), 1788–1793.

53 J. Yang and Y. Gao, A dipole-dipole interaction tuning the photoluminescence of silicon quantum dots in a water vapor environment, *Nanoscale*, 2019, **11**(4), 1790–1797.

54 A. K. Parchur, A. I. Prasad, A. A. Ansari, S. B. Rai and R. S. Ningthoujam, Luminescence properties of Tb^{3+}-doped $CaMoO_4$ nanoparticles: annealing effect, polar medium dispersible, polymer film and core–shell formation, *Dalton Trans.*, 2012, **41**(36), 11032.

55 H. Htoon, M. J. O'Connell, S. K. Doorn and V. I. Klimov, *Low-temperature, photoluminescence-excitation spectroscopy of individual carbon nanotubes*, in *2005 Quantum Electron. Laser Sci. Conf.*, IEEE, 2005, pp. 205–207.

56 C.-K. Duan, C.-C. Ko, G. Jia, X. Chen and P. A. Tanner, $^5D_3$–$^5D_4$ cross-relaxation of Tb^{3+} in a cubic host lattice, *Chem. Phys. Lett.*, 2011, **506**(4–6), 179–182.

57 S. Kuboniwa and T. Hoshina, Luminescent Properties of Tb^{3+} in Oxygen-Dominated Compounds, *J. Phys. Soc. Jpn.*, 1972, **32**(4), 1059–1068.

58 G. Liu, M. S. Molokeev, B. Lei and Z. Xia, Two-site Cr^{3+} occupation in the $MgTa_2O_6$:Cr3+ phosphor toward broadband near-infrared emission for vessel visualization, *J. Mater. Chem. C*, 2020, **8**(27), 9322–9328.

59 B. Bai, P. Dang, Z. Zhu, H. Lian and J. Lin, Broadband near-infrared emission of $La_3Ga_5GeO_{14}$:Tb^{3+},Cr^{3+} phosphors: energy transfer, persistent luminescence and application in NIR light-emitting diodes, *J. Mater. Chem. C*, 2020, **8**(34), 11760–11770.

60 K. Poria, S. Bhatia, R. Kashyap, V. Kashyap, I. Sihmar, N. Deopa and J. S. Shahi, Structural and luminescence properties of novel Eu^{3+}-doped $Na_3Ba_2LaNb_{10}O_{30}$ phosphors with high quantum efficiency and excellent color purity for w-LED applications, *RSC Adv.*, 2024, **14**(40), 29490–29504.

61 V. Singh, R. P. S. Chakradhar, J. L. Rao and H. Y. Kwak, Photoluminescence and EPR studies of $BaMgAl_{10}O_{17}$:Eu^{2+} phosphor with blue-emission synthesized by the solution combustion method, *J. Lumin.*, 2011, **131**(8), 1714–1718.

62 T. P. Gompa, S. M. Greer, N. T. Rice, N. Jiang, J. Telser, A. Ozarowski, B. W. Stein and H. S. La Pierre, High-Frequency and -Field Electron Paramagnetic Resonance Spectroscopic Analysis of Metal–Ligand Covalency in a $4f^7$ Valence Series (Eu^{2+}, Gd^{3+}, and Tb^{4+}), *Inorg. Chem.*, 2021, **60**(12), 9064–9073.

63 V. Singh, G. Sivaramaiah, N. Singh, M. S. Pathak, J. L. Rao, P. K. Singh and A. S. Nagpure, Ultraviolet B emission from a Gd^{3+}-doped $BaAl_2O_4$ powder phosphor, *Bull. Mater. Sci.*, 2019, **42**(1), 1–6.

64 E. Culea, L. Pop and S. Simon, Spectroscopic and magnetic behaviour of $xGd_2O_3(1-x)(Bi_2O_3{\cdot}PbO)$ glasses, *Mater. Sci. Eng. B*, 2004, **112**(1), 59–63.

65 T. Nakamura, K. Kaiya, N. Takahashi, T. Matsuzawa, C. C. Rowlands, V. Beltrán-López, G. M. Smith and P. C. Riedi, EPR investigations on europium(II)-doped barium aluminate, *Phys. Chem. Chem. Phys.*, 1999, **1**(17), 4011–4014.

66 V. Singh, G. Sivaramaiah, J. L. Rao and S. H. Kim, Optical and EPR properties of $BaAl_{12}O_{19}$:Eu^{2+}, Mn^{2+} phosphor prepared by facile solution combustion approach, *J. Lumin.*, 2015, **157**, 74–81.

67 V. Singh, R. P. S. Chakradhar, J. L. Rao and D. K. Kim, Photoluminescence and EPR studies of Cr-doped hibonite ($CaAl_{12}O_{19}$) phosphors, *Solid State Sci.*, 2008, **10**(11), 1525–1532.

68 Y. Wu, Y. Li, X. Qin, R. Chen, D. Wu, S. Liu and J. Qiu, Dual mode NIR long persistent phosphorescence and NIR-to-NIR Stokes luminescence in $La_3Ga_5GeO_{14}$:Cr^{3+},Nd^{3+} phosphor, *J. Alloys Compd.*, 2015, **649**, 62–66.

69 N. Mironova-Ulmane, A. I. Popov, G. Krieke, A. Antuzevics, V. Skvortsova, E. Elsts and A. Sarakovskis, Low-temperature studies of Cr^{3+} ions in natural and neutron-irradiated g-Al spinel, *Low Temp. Phys.*, 2020, **46**(12), 1154–1159.

70 T. Kinoshita, M. Yamazaki, H. Kawazoe and H. Hosono, Long lasting phosphorescence and photostimulated luminescence in Tb-ion-activated reduced calcium aluminate glasses, *J. Appl. Phys.*, 1999, **86**(7), 3729–3733.

71 S. K. Misra and S. Diehl, Theory of EPR lineshape in samples concentrated in paramagnetic spins: Effect of enhanced internal magnetic field on high-field high-frequency (HFHF) EPR lineshape, *J. Magn. Reson.*, 2012, **219**, 53–60.

72 Y. Wei, Z. Gao, X. Yun, H. Yang, Y. Liu and G. Li, Abnormal Bi^{3+}-Activated NIR Emission in Highly Symmetric $XAl_{12}O_{19}$(X = Ba, Sr, Ca) by Selective Sites Occupation, *Chem. Mater.*, 2020, **32**(19), 8747–8753.

73 L. W. Zhang, L. Wang and Y. F. Zhu, Synthesis and performance of $BaAl_2O_4$ with a wide spectral range of optical absorption, *Adv. Funct. Mater.*, 2007, **17**(18), 3781–3790.

74 V. Pagonis, The effect of annealing atmosphere on the thermoluminescence of synthetic calcite, *Radiat. Meas.*, 1998, **29**(1), 45–52.

75 S. Blahuta, A. Bessière, B. Viana, V. Ouspenski, E. Mattmann, J. Lejay and D. Gourier, Defects Identification and Effects of Annealing on $Lu_{2(1-x)}Y_{2x}SiO_5$ (LYSO) Single Crystals for Scintillation Application, *Materials*, 2011, **4**(7), 1224–1237.

76 G. Kitis, J. M. Gomez-Ros and J. W. N. Tuyn, Thermoluminescence glow-curve deconvolution functions for first, second and general orders of kinetics, *J. Phys. D: Appl. Phys.*, 1998, **31**(19), 2636–2641.